Additive Manufacturing 97 (2025) 104614

Contents lists available at ScienceDirect

Additive Manufacturing

journal homepage: www.elsevier.com/locate/addma

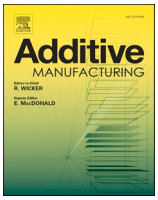

The selection of scanning strategy and annealing schedule for the optimization of texture and magnetic properties of Fe-3.5 wt%Si alloy parts fabricated by laser powder bed fusion

Fanbo Meng [a], Konstantinos A. Liogas [b,c], Kwang Boon Lau [c], Yuheng Deng [d], Alexander M. Korsunsky [b], Pei Wang [c,e], Xiaojun Shen [a], Christopher H.T. Lee [a,*]

[a] School of Electrical and Electronic Engineering, Nanyang Technological University, 50 Nanyang Avenue, Singapore 639798, Singapore
[b] MBLEM, Department of Engineering Science, University of Oxford, Parks Road, Oxford OX1 3PJ, United Kingdom
[c] Institute of Materials Research and Engineering (IMRE), Agency for Science Technology and Research (A*STAR), 2 Fusionopolis Way, Innovis #08-03, 138634, Singapore
[d] School of Materials Science and Engineering, Nanyang Technological University, 50 Nanyang Avenue, 639798, Singapore
[e] Engineering Cluster, Singapore Institute of Technology, 519961, Singapore

ARTICLE INFO

Keywords:
Additive manufacturing
Laser powder bed fusion (LPBF)
Electrical steel
Scanning strategy
Texture
Abnormal grain growth
Magnetic properties

ABSTRACT

By careful selection of the scanning strategies (SS), researchers in this study were able to realize a simple algorithm to control the grain orientation with the extremely strong Rotated Cube and Cube texture obtained in laser powder bed fusion (LPBF) fabricated electrical steel. Microstructure was characterized by optical microscopy (OM) and electron backscatter diffraction (EBSD), and quasi-static magnetic properties were measured through DC closed magnetic circuit method. The findings show that sufficient remelting with a stable thermal field induces a strong < 001 > parallel to the building direction (BD) texture by promoting epitaxial growth aligned with BD. In-plane grain orientation rotates from < 011 > //X-axis towards < 001 > //X-axis (X-/Y-axis denote length/width directions of samples, respectively) with the reduction of the track length. By promoting < 001 > //BD and < 001 > //X-axis textures, double scanning introduced a strong Cube texture in the D-XY samples (double scan along X-axis and Y-axis successively in one layer). Sample heat treatment (HT) considered in this study only induced abnormal grain growth. Coarse grains and desirable texture components contribute to improving permeability during magnetization of domain wall displacement and rotation of the magnetization vector, respectively, and coarse grains also reduce coercivity (H_c). Benefitting from corresponding microstructure, D-XY samples annealed at 1000℃ for 2 h exhibited the highest maximum relative permeability (μ_{rmax}) of 4450, while S-X samples (single scan along X-axis) annealed at 1150℃ for 4 h showed the highest initial permeability (μ_i) of 0.34 mH/m and lowest H_c of 44.5 A/m in this study. This study provides an insight into the relationship between the manufacturing route, microstructure, and magnetic properties of LPBFed electrical steel and establishes a firm basis for controlling the texture components and grain morphology of Fe-3.5 wt%Si via judicious selection of SS and HT.

1. Introduction

Electrical steel, also called silicon steel, for several decades has been the principal engineering choice of soft magnetic material in electric machines and is commonly used to fabricate electromagnetic components (such as iron cores in electric motors). Its excellent saturation induction, permeability, low coercivity, and high electrical resistivity in combination with a relatively low cost make it an ideal candidate for electrical machine applications [1–7]. Recent advancements in metal additive manufacturing (AM), specifically laser powder bed fusion (LPBF), have presented new opportunities for these well-developed materials and electric machines [8–11]. LPBF's ability to create complex structures has opened up new possibilities for designing and fabricating lightweight motors with customized functionalities, showing

* Correspondence to: School of Electrical and Electronic Engineering, Nanyang Technological University, S2-B2c-101, 50 Nanyang Avenue, Singapore 639798, Singapore.
E-mail address: chtlee@ntu.edu.sg (C.H.T. Lee).

https://doi.org/10.1016/j.addma.2024.104614
Received 2 June 2024; Received in revised form 27 November 2024; Accepted 16 December 2024
Available online 17 December 2024

the potential to expand the range of applications for electric motors beyond traditional uses [12].

The soft magnetic properties of electrical steel are strongly dependent on the microstructure. The presence of residual stress, defects, precipitates, and impurities can affect the domain wall movement during the magnetization/demagnetization process, leading to a degree of magnetic hardening reflected in lower maximum relative permeability (μ_{rmax}) and higher coercivity (H_c) [5–7]. Secondly, the grain crystallographic orientation may have a great effect on the magnetization response since in a body-centered-cubic (BCC) structure the easy magnetization axis is associated with the $< 001 >$ direction, while the hard axis of magnetization lies along $< 111 >$ [5–7]. Consequently, according to the texture components present, electrical steel is typically categorized as grain-oriented (GO) and non-oriented (NO) types. Thirdly, the grain size also plays a role in affecting the values of μ_{rmax} and H_c. Based on the Grain Size Dependence of Coercivity and Permeability (GSDCP) theory, the enlargement of grain size exceeding the domain wall width can reduce H_c as well as improve μ_{rmax}, where the domain wall width of the ferromagnets can be calculated from $\delta_B = \pi\sqrt{\frac{A}{K_1}}$ (δ_B, A, and K_1 are the domain wall width, exchange constant, and magnetocrystalline anisotropy constant, respectively) [13–17]. The typical domain wall width of ferromagnets is tens of nanometers, which is much smaller than grain sizes of electrical steels [13–17].

Previous research on electrical steel primarily focused on investigating the microstructure evolution during conventional fabrication processes (i.e., casting, rolling, and annealing), aiming to obtain desired crystallographic texture components and grain sizes [18–34]. In general, during solidification, the texture is often dominated by the texture with $< 001 >$ direction parallel to the normal direction (i.e., θ-fiber texture) due to the $< 001 >$ solidification direction in the BCC structure [18–21]. Subsequent plastic deformation in the rolling process induces a rotation of crystallographic orientation, leading to the development of the texture with $< 011 >$ direction parallel to the rolling direction (i.e., α-fiber texture) and the texture with $< 111 >$ direction parallel to the normal direction (i.e., γ-fiber texture) at the expense of the θ-fiber texture [20–22]. Song et al. [22] found that this change in the dominant texture can be intensified by increasing the hot rolling reduction, especially, a strong Goss texture was observed when the reduction reached 50 %. For the last annealing process, researchers such as Sha et al. [20], Liang et al. [23], and Jiao et al. [21] found that the suitable annealing conditions can revert α- and γ-fiber textures back to θ-fiber texture through the oriented nucleation mechanism of recrystallization. This shift in the major texture type is often accompanied by abnormal grain growth (AGG) of Goss grains. The AGG phenomenon may be mostly attributed to the more frequent occurrence of Coincident Site Lattice (CSL) boundary between Goss grains and 35°-45° large angle grain boundaries between Goss grains and γ-fiber texture grains in rolled microstructure, where the higher mobility of these two types of grain boundaries allows Goss grains to initiate growth with a lower driving force [24–28]. The pinning effect of grain boundary precipitates further enhances this advantage, ultimately leading to AGG of Goss grains [24–29]. Notably, recent research by Birosca et al. [35] suggested that the differences in the thermal conductivity along specific crystal planes may also contribute to the AGG of Goss grains. Specifically, the higher thermal conductivity along the (011) plane in the BCC structure is advantageous for abnormal growth when more (011) planes are parallel to the heat flux during annealing in Goss grains.

For LPBF-manufactured electrical steel, several methods have been explored to control grain orientation distributions, such as adjusting processing parameters [36–41], annealing [42], and in-source beam shaping [43]. Macknojia et al. [38] and Galbusera et al. [43] successfully obtained $< 001 >$ //BD fiber texture through optimizing the processing parameters and in-source beam shaping, respectively. Although Stornelli et al. claimed to have achieved the Cubic texture in Fe-3.0 wt% Si and Goss texture in Fe-6.5 wt%Si by controlling the processing parameters and annealing process, their determination of these textures was based solely on XRD results from the cross-section parallel to BD [42]. Not only in electrical steels, Ahmadnia et al. also achieved the texture of $< 111 >$ paralleling to the magnetic field in Fe-50Ni alloy by controlling both processing parameters and annealing process [44]. It could be found that the above methods can only align the grain orientations with a single direction (usually BD) but not multi-directions, thus only fiber textures were obtained.

To further realize the control of crystallographic texture components in LPBF, searching for a suitable scanning strategy (SS) may hold potential. For example, Nadammal et al. [45] demonstrated that compared to the alternating SS, the rotational SS formed more complex thermal fields, thus introducing a more random distribution of grain orientations. Marattukalam et al. [46] fabricated the 316 L stainless steel samples with a bidirectional SS without rotation and obtained a strong $< 100 >$ and $< 110 >$ single crystalline-like texture along the scanning direction (SD) and building direction (BD), respectively. Sun et al. [47] successfully obtained a single-crystalline-like texture with a short-range order of Mo atoms in Ni-25 at% Mo alloys by using both bidirectional scanning along one axis (X-scan) and bidirectional scanning with a 90° rotation in each layer (XY-scan). Regarding the LPBF-manufactured silicon steel, Haines et al. [48] reported achieving different textures by using longitudinal and transverse SS, however, the texture strength was relatively low and the corresponding magnetic properties were not measured. Through simulation, they demonstrated that the formation of different textures was primarily due to the variations in the thermal field under these two SS. This finding can provide a way of thinking that modifying the thermal field of molten pools by designing SS could be a potential approach to achieve desired textures. However, most studies to date into microstructure control during LBPF have been devoted to structural materials and primarily concerned the mechanical properties influenced mostly by the structural defects (porosity, associated cracks), rather than by crystallographic texture [49–54]. Residual stress in LPBF-manufactured components was shown to be affected by SS [55,56], hence the research largely focused on finding suitable SS to reduce the residual stress, leading to the introduction of the island SS (also called chessbox) SS now [51–56].

For the LPBF-fabricated soft magnetic materials, the optimized heat treatment (HT) remains the first option to increase the grain size. Liogas et al. [57] obtained the LPBF-manufactured Fe-Co alloy with notably soft magnetic properties (μ_{rmax} = 8197, H_c = 112 A/m) introduced by optimizing HT, which were found to be superior to commercial products HIPERCO® 50 A [58] and VACOFLUX 50 [59]. They also demonstrated that these superior soft magnetic properties were induced by the combination of large grain size and chemical ordering. In terms of LPBF-fabricated electrical steel, the work on improving the magnetic properties through grain growth was also reported in some studies [38–41,60,61], but the aforementioned relationship was not sufficiently clarified. On the other hand, the magnetic properties of additively manufactured brittle electrical steels (e.g., high-silicon-content electrical steel) may also deteriorate due to grain boundary cracking during grain growth, which Adamczyk et al. observed this cracking phenomenon and successfully mitigated it by applying suitable scanning strategies (SS) and annealing conditions [62].

In summary, there is limited research conducted on LPBF of electrical steel, with little emphasis on controlling the crystallographic orientations and a lack of in-depth investigation into the influence of microstructural characteristics on the soft magnetic properties. The present work aims to control the orientation of grains via SS and to elucidate the distinct effects of various microstructural characteristics on the magnetic properties of LPBF-fabricated electrical steel. The results seek to identify possible manufacturing routes to improve the electrical motor performance through the introduction of the easy magnetization axis induced by additive manufacturing within the microstructure of soft electromagnetic components that allows aligning with the designed

magnetic flux. Furthermore, the identification of the optimized heat treatment that promotes AGG allows further improvement in the performance of these components.

2. Materials and experiments

2.1. Materials

Pre-alloyed gas-atomized spherical Fe-3.5Si (wt%) powder (supplied by Coatecs Pte. Ltd., Singapore) with the diameter range of 15–35 μm was used to fabricate bulk samples via LPBF. Detailed morphology and chemical composition of the powder can be found in [37]. The phase diagrams of the Fe-Si binary system assessed by [63] are provided in Fig. S1, which demonstrates that the materials used in this study are the single phase. The LPBF fabrication was conducted on a TruPrint 1000 (TRUMPF SE + Co. KG) equipped with a 200 W TRUMPF fiber laser with 1070 nm wavelength and 30 μm laser beam spot size. The scanning parameters were set to the laser power of 150 W, scanning speed of 400 mm/s, hatching space of 90 μm, and layer thickness of 20 μm. The above scanning parameters were selected based on the authors' work [37], in which the parts fabricated with the above parameters achieved a high relative density (i.e., 99.9 %) and also developed an extremely strong < 001 > //BD fiber texture. In the coordinate system shown in Fig. 1, this < 001 > //BD texture not only ensures the distribution of the < 001 > (easy axis) within the XY-plane, but also prevents the formation of < 111 > (hard axis) in the XY-plane. Two types of samples, i.e., thin-wall-structure pillars (10 mm (L) × 1.5 mm (W) × 50 mm (H)) and square cores (24 mm (inner side length) × 27 mm (outer side length) × 6 mm (H)) were fabricated with various SS for microstructure characterization and quasi-static magnetic testing, respectively. All the samples were fabricated without the borders. All the SS applied to fabricate the pillars are illustrated in Fig. 1 with their designations in this study, where "S-" and "D-" refer to laser scanning once and twice in each single layer, respectively. S-X/Y is the same as the most used island SS with an island size of 5 mm × 5 mm and scan rotation of 67° after every successive layer was used. S-X and S-Y were scanned along the X-axis and Y-axis, respectively. "D-" samples can be considered as combining S-X and S-Y in the single layer, where laser scanned along the X-axis first and then the Y-axis in D-XY while D-YX was the reversed order of X- and Y-axis. S-X/Y, S-X, and D-XY sequences were also selected to fabricate square cores, in which each side of the square core was assumed to be one thin-wall-structure pillar so that the S-X and D-XY could be applied.

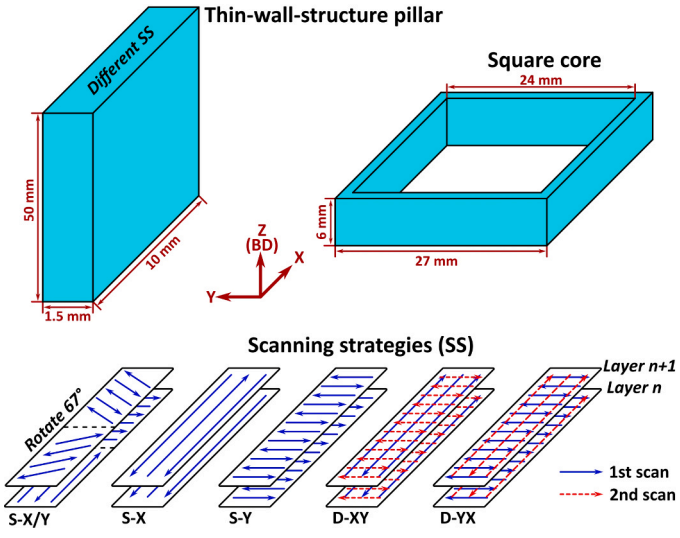

Fig. 1. Geometries of thin-wall-structure pillars and square cores, and schematic for different axes and all the scanning strategies with their denotations used in this study.

After fabrication, the samples were removed from the substrate plate using electrical discharge machining (EDM). Heat treatment (HT) was conducted in a muffle furnace with nitrogen (N_2) used as the protective gas. HT was chosen to provide a simple one-step annealing process (heating-soaking-cooling) by using the heating rate of 5 ℃/min followed by furnace cooling. The soaking temperatures included 1000℃, 1100℃, 1150℃, and 1175℃, and the soaking time was set to 2 h, 4 h, and 6 h. The combinations of soaking temperature and time are labeled in the related figures.

2.2. Microstructure characterization

The morphology of the molten pools (MP) was obtained by observing it under an optical microscope (DSX1000 Digital Microscopes). The top morphology (XY-plane) was captured directly from the top surface of the as-fabricated (AF) samples. To obtain the side morphology (YZ-plane) of MP, the samples were mounted in conductive resin, then the side surface was prepared using standard metallographic techniques and oxide polishing suspension to obtain a mirror surface finish, and finally etched with 3 % Nital for approximately 40 seconds. Microstructural analysis of the grain orientations was performed using electron backscattered diffraction (EBSD) in a field emission scanning electron microscope (FESEM, JEOL JSM-7800F PRIME) with step sizes of 0.117 μm (Fig. 8) and 1.95 μm (other EBSD maps). The post-analysis of EBSD data was performed by AZtecCrystal software (Oxford Instruments Nano-Analysis), in which the half-width for the calculation of both inverse pole figures (IPF) and orientation distribution function (ODF) was defined as 10°.

2.3. Quasi-static magnetic property testing

The quasi-static magnetic properties were tested using closed-circuit methods under direct current (DC) based on ASTM standard (ASTM A773/A773M-21) [64]. The samples were first thinned by around 0.25 mm from both inner and outer contours by EDM to smooth the surface and remove the oxidation layer of HT samples. The quasi-static magnetic testing was performed on a MATS-2010SD (HUNAN LINKJOIN TECHNOLOGY CO., LTD.). The primary and secondary windings of the samples were 80 and 40 turns, respectively, and the samples were demagnetized before each test. The magnetic field (H) was applied along the contour direction of the square samples with a maximum strength of 3000 A/m. Except that the μ_r-H curve and maximum relative permeability (μ_{rmax}) were derived by calculating the slope of the magnetization curve, all the other data (including magnetization curve, hysteresis loop, magnetic flux at 3000 A/m (B_{3000}), remanence (B_r), and coercivity (H_c) were directly provided by the machine.

3. Results

3.1. Influence of scanning strategies on texture

Fig. 2 displays the grain orientations of AF samples observed from the cross-sections perpendicular to BD (i.e., XY-plane). The out-of-plane and in-plane features of grain orientations are characterized by IPF-colored EBSD maps with respect to BD (Fig. 2 (1)) and X-axis (Fig. 2 (2)), respectively, and the corresponding IPF intensity sets are shown in Fig. 2 (3).

The distributions of grain orientations with respect to BD as presented in Fig. 2 (1) generally show a dependency on the sample regions, namely, the shell and the core. Through the blue-red-blue pattern of IPF color in Fig. 2 (1), it can be ascertained that grains located at the shell of the samples tend to align with non-< 001 > crystalline orientations parallel to BD, while the core regions are dominated by the grains with < 001 > //BD, forming a strong θ-fiber texture. The influence of different SS on the out-of-plane features mainly reflects on the area

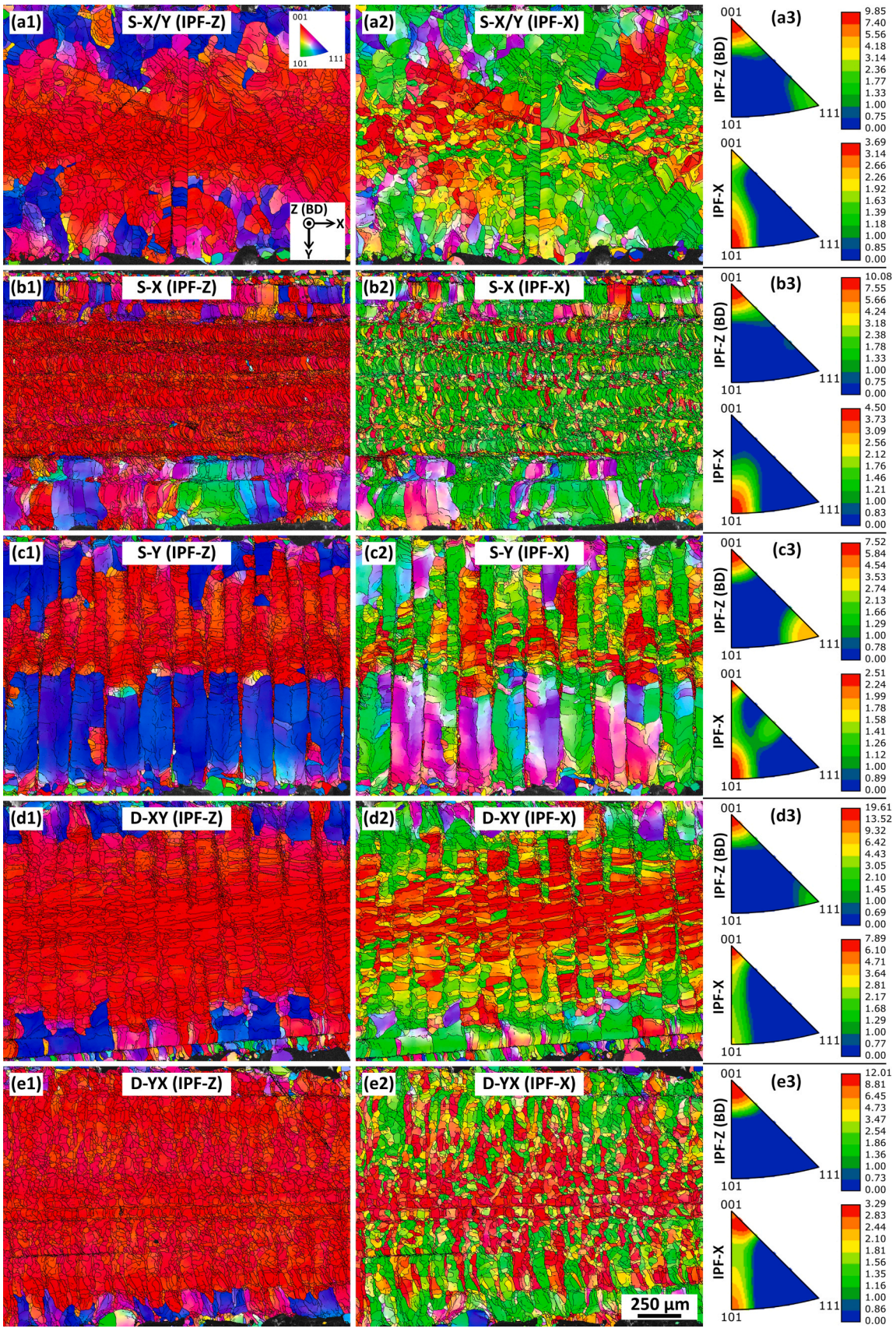

Fig. 2. (1)-(2) are the EBSD maps of AF samples in the XY-plane with IPF-Z coloring and IPF-X coloring, respectively, and (3) are the corresponding inverse pole figures (IPF) sets. (a)-(e) represents S-X/Y, S-X, S-Y, D-XY, and D-YX, respectively.

fraction of the shell and the core. In the single-scanned samples, the shell regions occupy a considerable fraction, especially, in S-Y, with the non-< 001 > //BD texture being enhanced into a strong < 111 > //BD texture (i.e., γ-fiber texture) on almost half of the cross-sectional area. On the other hand, it was shown that additional scanning in the double-scanned samples can effectively reduce the area fraction of the shell region, with only a few non-< 001 > //BD grains detected in D-XY and D-YX samples. The analysis of the in-plane features reveals the dominance of the θ-fiber texture in the core region. In the single-scanned samples, the in-plane feature represented in Fig. 2 (a2-c2) shows a relationship with the scanning track length. As the scanning track length reduced from S-X to S-Y, the grain orientation with respect to the X-axis shifted from < 011 > to < 001 > at the core of the samples. This change in preferred orientation with respect to the X-axis is also evident through the appearance of < 001 > peak and the reduced MUD value of < 011 > in IPF-X set from Fig. 2 (b3) to (c3). It should be noticed that this shifting of preferred grain orientation also applies to the scanning coordinating system (SD-Width-BD) due to its geometric relationship with the sample coordinating system (X-Y-Z in Fig. 1). Therefore, the grain orientation with respect to SD also changed from < 011 > to < 001 > with the reduction of scanning track length.

Particularly, in S-Y, on one hand, it is good to see that < 001 > //X-axis was formed stably in the core of the samples, which offers the potential to align the easy axis with the applied magnetic field when designing magnetic testing samples. On the other hand, it is inefficient to align the easy axis with the applied magnetic field with a single scanned SS, since only the limited numbers of the grains with < 001 > //X-axis can be found in S-Y. Consequently, the enlarged area of < 001 > //X-axis in Fig. 2 (d2, e2) and notable increase of the MUD value of < 001 > in Fig. 2 (d3, e3) shows that the usage of double scanning can overcome this problem. Particularly, in D-XY, the area of the sample exhibiting < 001 > //X-axis was substantially enlarged, resulting in the highest MUD value of 7.89 for < 001 > //X-axis — almost twice that of the other SS.

To further clarify the texture features, an inspection of texture components was additionally conducted based on Fig. 2 by calculating the ODF maps (Fig. 3) and quantifying the area fraction of each texture component (Fig. 4). In general, the pronounced intensity distribution along the θ-fiber axis in Fig. 3 with it constituting over 50 % of the area fraction in Fig. 4 further confirms that the θ-fiber texture is the predominant texture type in this study (except in the S-Y samples). Additionally, the strong {001}< 110 > (Rotated Cube texture) and {001}< 100 > (Cube texture) were detected in the S-X sample and the D-XY sample, respectively, both of them account for around one-third of the cross-sectional area.

Since the S-X sample and the D-XY sample exhibited pronounced and distinctive texture components, they were selected for the following study about annealing and quasi-static magnetic testing. S-X/Y, as the mostly used SS in LPBF research, was also included in the comparison.

3.2. Influence of annealing on microstructure

The HTed microstructure is shown in Fig. 5 through IPF-X colored EBSD maps, where (a)-(c) correspond to the samples manufactured by using S-X/Y, S-X, and D-XY, respectively, and (1)-(3) represent the HT conditions of 1000℃ for 2 h, 1100℃ for 2 h, and 1150℃ for 2 h, respectively. The investigation of the HT microstructure will primarily focus on two critical aspects: grain size (including grain growth) and texture components because both are key factors influencing magnetic properties.

Compared to Fig. 2, the HTed microstructure in Fig. 5 demonstrates the effects of HT varied among the different SS-fabricated samples. When the samples underwent annealing at 1000℃ for 2 h or 1100℃ for 2 h (Fig. 5 (a1-c2)), the microstructure remained unchanged from the AF condition with no visible grain growth. Thus, it can be inferred that only the recovery occurred without the visible recrystallization under these two HT conditions. This finding deviates from previous research on HTed microstructure of the LPBFed electrical steel [40,41,48,60,61]. As compared to the AF microstructure in these studies, the AF microstructure in this study exhibits larger grain sizes and stronger texture. Under this condition, the surface energy is already minimized [33,35,65], and the occurrence of high energy boundaries (defined as boundaries between grains misorientated by the angle of 20°-45°) with higher mobility is significantly reduced [25–27,34,35]. Therefore, less driving

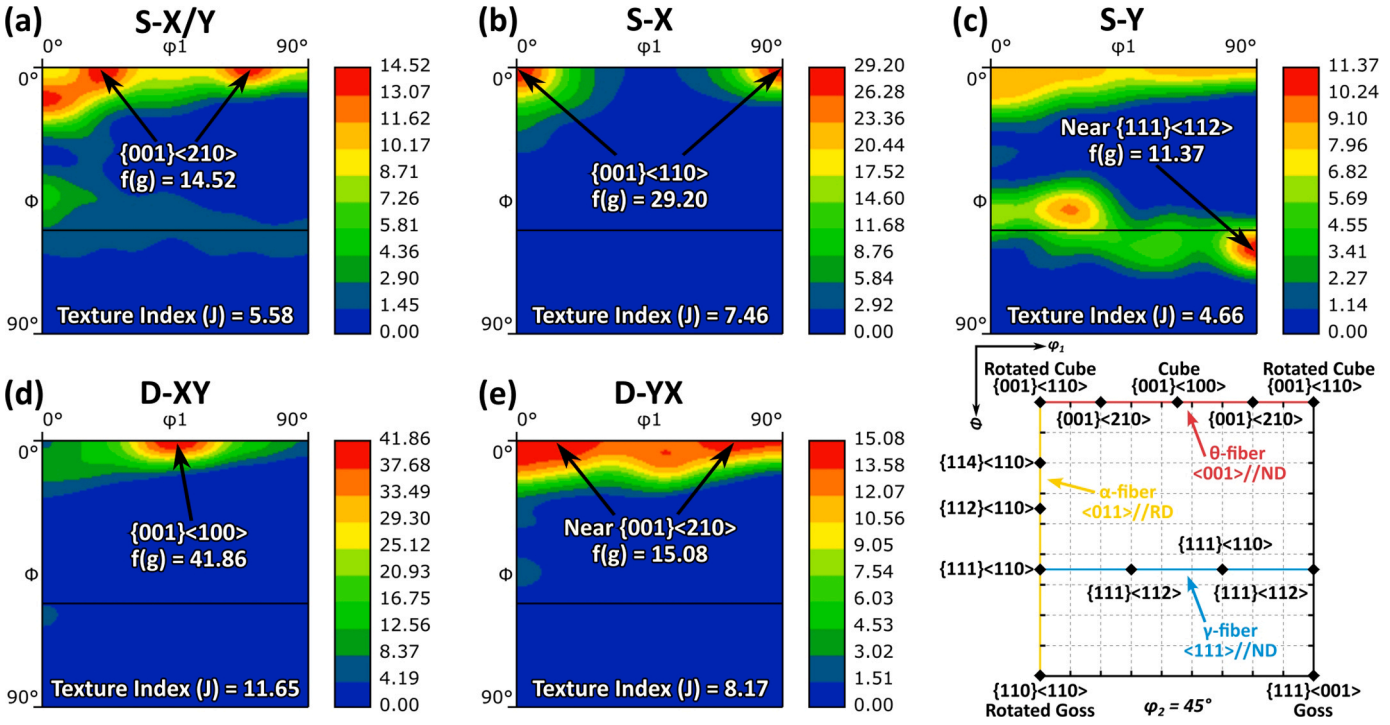

Fig. 3. $\varphi_2 = 45^\circ$ section of ODF maps calculated from the Fig. 2.

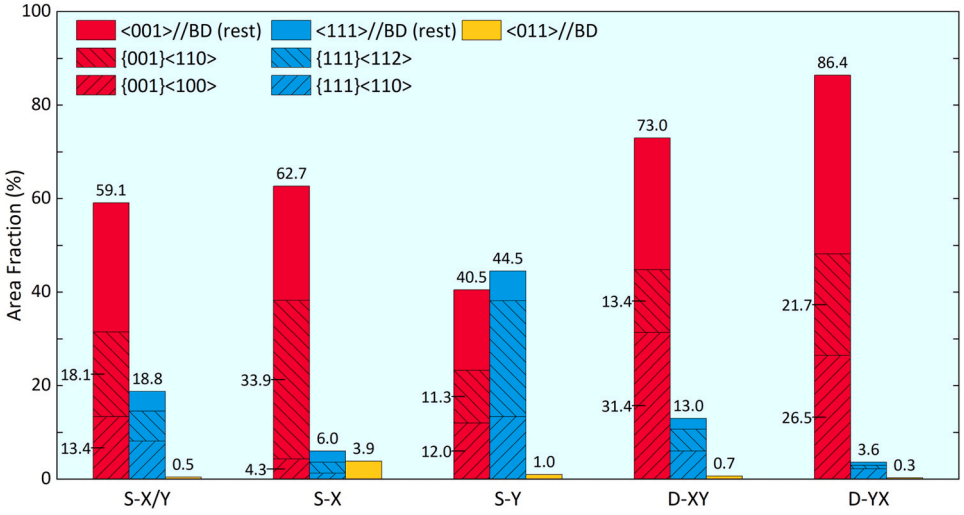

Fig. 4. The statistics of the area fractions of selected texture components in Fig. 2, where the deviation angles for each texture component were set as 15°.

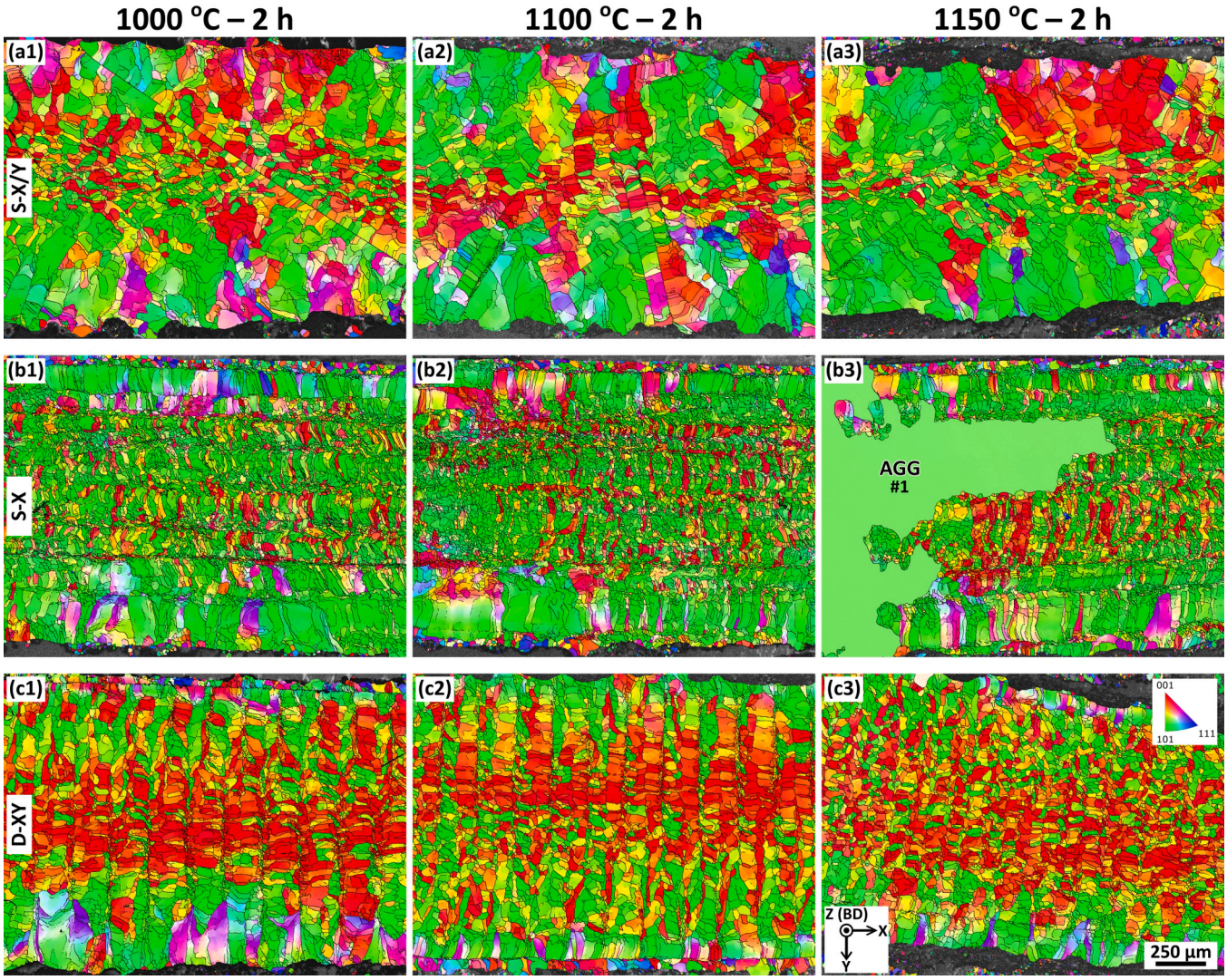

Fig. 5. EBSD maps of HTed samples in XY-plane with IPF-X coloring, where (a)-(c) represent S-X/Y, S-X, and D-XY, respectively, and (1)-(3) refer to HT conditions of 1000℃ for 2 h, 1100℃ for 2 h, and 1150℃ for 2 h, respectively.

force can be provided for grain growth in this study [25–27,33–35,65], which is the possible reason for the differing findings to previous studies mentioned above. The texture components of the samples HTed under 1000℃ for 2 h were evaluated by using the ODF images calculated from Fig. 5 (a1, b1, and c1), which are shown as Fig. 6. The high intensity of {001}< 110 > and {001}< 100 > in Fig. 6 demonstrates their remained dominance in the S-X sample and the D-XY samples, respectively, suggesting no texture evolution under these two HT conditions, too. However, as the HT temperature increased to 1150℃, the different effects of HT on the microstructure of different SS-fabricated samples were observed. In the S-X/Y sample and the D-XY sample, both the grain size and texture still remained consistent with the AF condition, while a notable occurrence of AGG was observed in the S-X sample, as evidenced by the labeled coarse grain in Fig. 5 (b3).

To further investigate the phenomenon of AGG in the S-X samples, additional HT conditions were applied to the AF S-X samples, and the corresponding microstructure is illustrated in Fig. 7. Upon comparing the microstructure shown in Fig. 5 and Fig. 7, it can be deduced that grain growth (i.e., recrystallization) occurred primarily through the mechanism of AGG, with no instances of normal grain growth (NGG) observed.

Under the HT temperature of 1150℃ in Fig. 7, although the coarse AGG grains already became the dominant grain type in the cross-section of the samples, the other regions within the cross-section retained the same microstructure as the AF condition (i.e., matrix grains). Even when the AGG was further promoted by the increasing of the HT temperature with an exceeding 0.5 mm grain size of the AGG grain, the matrix grains were still not all consumed by the AGG grains, as indicated by the black-circled regions in Fig. 7 (d). Besides, it should be noticed that after the AGG reached an extent under a certain HT temperature (from Fig. 5 (b3) to Fig. 7 (a)), the additional increase in HT time could neither promote the growth of AGG grains nor expand the area fraction of AGG grains in the cross-section (as compared Fig. 7 (b) to (a)). Finally, even though the HT temperature was raised to 1175℃ with the HT time expended to 4 h, AGG grains had yet to entirely replace the matrix grains, in other words, a 100 % AGG microstructure was not achieved in this research.

To assess the uniformity of the microstructure within AGG grains and matrix grains, the Kernel Average Misorientation (KAM) map of the S-X sample HTed under 1175℃ for 4 h is presented in Fig. 8 (a), with the variation of misorientations along A-A' (inside the AGG grain) and B-B' (inside matrix grains) plotted in Fig. 8 (b). Notably, the AGG grain exhibited a relatively uniform microstructure internally, characterized by a low KAM level and nearly 0° misorientation variation inside. In contrast, a higher misorientation level was detected within the matrix grains due to the existence of substructures. To clarify if there is a preferred grain orientation of AGG (i.e., recrystallization texture), the grain orientations of AGG grains were extracted and presented in Table 1. According to Table 1, the AGG grains neither display a strong tendency to inherit grain orientations from the matrix grains nor develop a distinct new preferred orientation. Unlike the highly textured matrix grains, the AGG grains exhibited a relatively random distribution of the grain orientations. It should be declared that the mechanisms underlying AGG (such as occurrence conditions, nucleation, grain boundary movement, etc.) are not the primary research focus of this study, so an in-depth investigation into the AGG phenomenon was not pursued.

Finally, two kinds of HTed microstructure were obtained in this study: (1) the microstructure remained the same as the AF condition (i.e., 100 % matrix grains), and (2) the microstructure with the dominated AGG grains and a few matrix grains.

3.3. Quasi-static magnetic properties

The quasi-static magnetic properties were investigated with the AF samples and the HTed samples. The selected HT conditions were 1000℃ for 2 h (denoted as HT-1) and 1150℃ for 4 h (denoted as HT-2). Since the AGG grains were only observed in the HTed S-X sample, HT-2 was exclusively conducted on the S-X sample. The magnetization characteristics and hysteresis loop of the AF and HTed samples are presented in Fig. 9 and Fig. 10, respectively. Additionally, a visual comparison of several key quasi-static magnetic properties is provided in Fig. 11, with the detailed values listed in Table 2.

Compared to the HTed samples, the AF samples show extremely low μ_r and B_{3000}, and doubled H_c, suggesting their considerable resistance to magnetization and demagnetization. This hard magnetic response of the AF samples was then greatly softened by the HT. Especially, even though neither the grain growth nor the texture evolution happened during HT-1, the HT-1 samples exhibited much softer magnetic behavior than the AF samples, which is characterized by the remarkable increase in μ_r and B (Fig. 9), and a halving of H_c (Fig. 10). Furthermore, the HT-1 D-XY sample, benefiting from its pronounced < 001 > //H texture, exhibited the superior fast magnetic response, which can be determined from its relatively high μ_r in Fig. 9 (c). Especially, the highest $\mu_{rmax} = 4450$ in this research was also obtained in the HT-1 D-XY sample (as shown in Fig. 11 and Table 2), approximately 18 % higher than that of the HT-1 sample fabricated with SS of S-X/Y (the mostly used SS in the LPBF research).

Compared to the HT-1 samples, the formation of coarse AGG grains in the HT-2 S-X introduced additional modifications to the quasi-static magnetic characteristics in some aspects. On one hand, the coarse AGG grains further reduced the magnetic hardness at the weak H field (H ~< 50 A/m), where the HT-2 S-X sample exhibited the highest μ_r in Fig. 9 (d). This softening effect of the coarse AGG grains on the magnetic behavior also enabled the HT-2 S-X sample to achieve the lowest H_c = 44.5 A/m and B_r = 0.390 T in this research (Fig. 11 and Table 2). On the other hand, this fastest magnetic response of the HT-2 S-X sample was not kept at the entire H field with a significant reduction of μ_r as H beyond around 50 A/m, as shown in Fig. 9 (c). As a result, the HT-2 S-X sample also exhibited the lowest B_{3000} = 1.493 T and μ_{rmax} = 3692 among all the HTed samples.

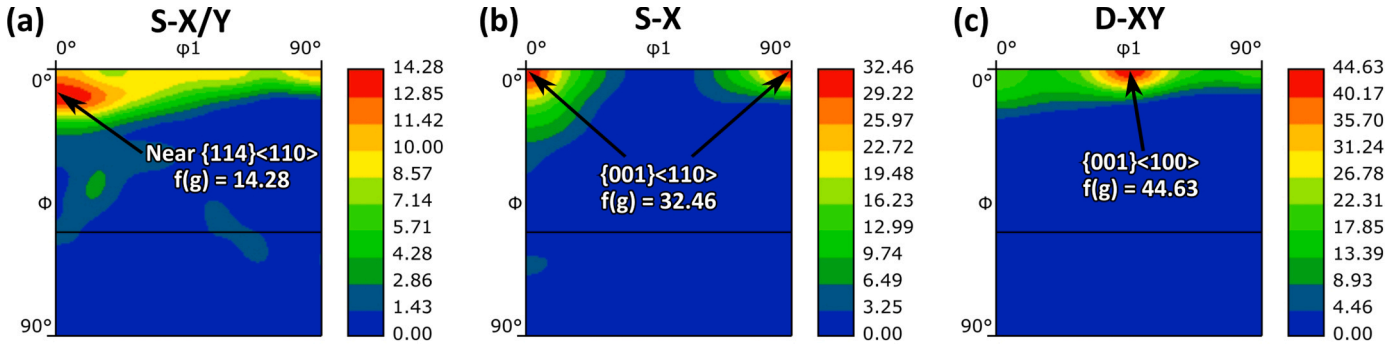

Fig. 6. $\varphi_2 = 45°$ section of ODF maps calculated from the Fig. 5 (a1)-(c1).

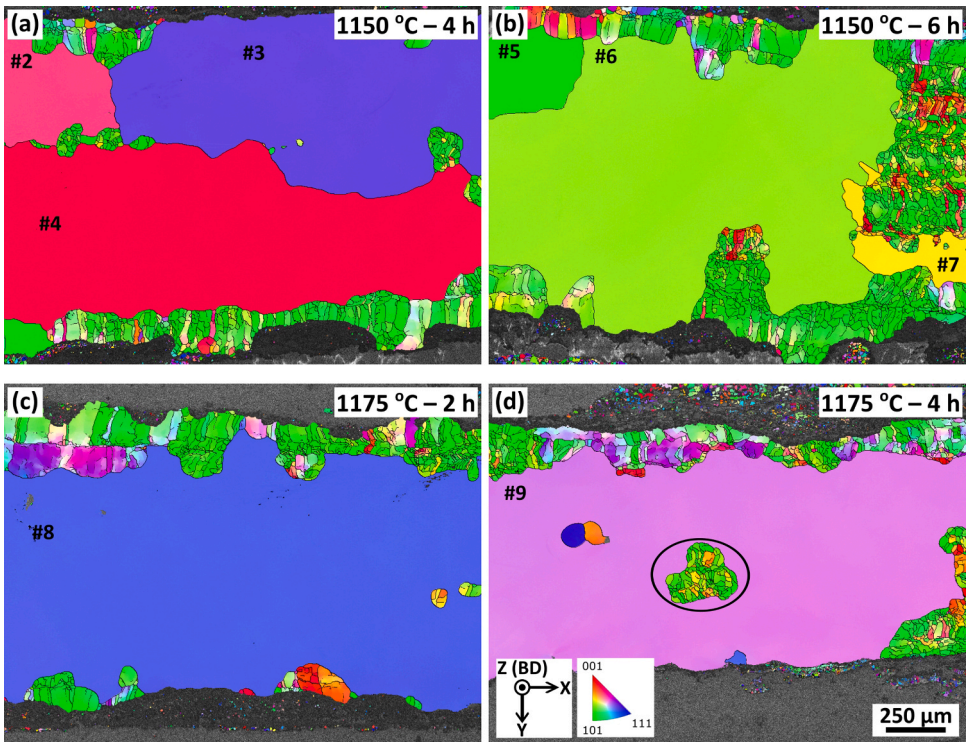

Fig. 7. EBSD maps of HTed S-X in XY-plane with IPF-X coloring, where HT conditions in (a)-(d) are 1150℃ for 4 h, 1150℃ for 6 h, 1175℃ for 2 h, and 1175℃ for 4 h, respectively.

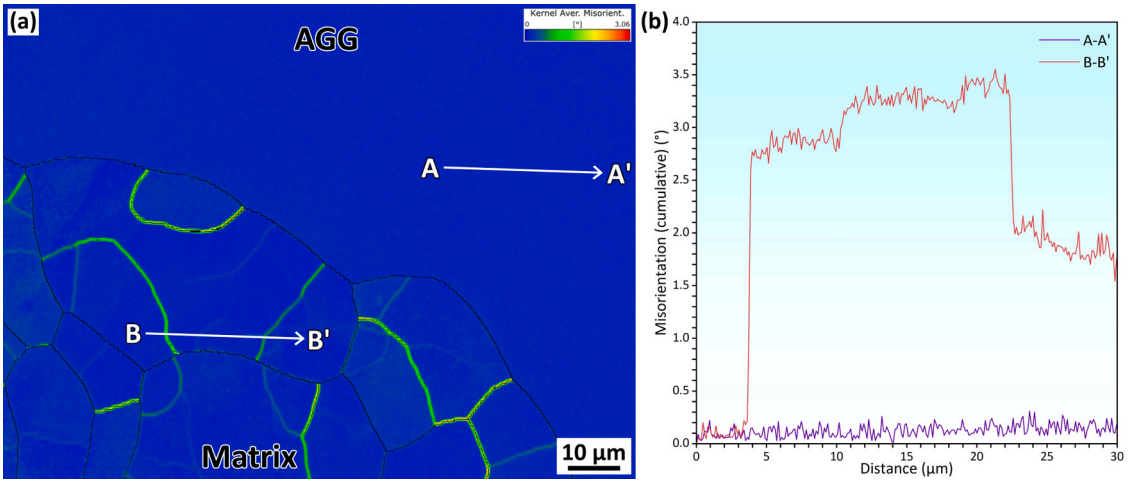

Fig. 8. (a) the Kernel average misorientation (KAM) map of the S-X sample annealed under 1175℃ for 4 h, (b) shows the cumulative misorientation distribution along the arrows in (a).

Table 1
Grain orientations of the labeled AGG grains in Fig. 5 and Fig. 7.

Grain No.	Euler angles			The closest grain orientations with respect to		
	Φ_1 (°)	φ_2 (°)	Φ_3 (°)	X-axis	Y-axis	Z-axis
#1	26.26 (± 0.27)	17.58 (± 0.10)	31.95 (± 0.38)	< 3–41 >	< 32–1 >	< 114 >
#2	31.90 (± 0.17)	36.89 (± 0.11)	51.68 (± 0.15)	< 1–41 >	< 30–2 >	< 112 >
#3	58.80 (± 0.14)	26.50 (± 0.09)	1.04 (± 0.11)	< 3–42 >	< 42–1 >	< 012 >
#4	158.57 (± 0.24)	20.99 (± 0.20)	8.99 (± 0.25)	< −4–11 >	< 1–31 >	< 013 >
#5	179.29 (± 0.90)	6.96 (± 0.26)	48.28 (± 0.89)	< −110 >	< −4–41 >	< 001 >
#6	126.89 (± 0.27)	40.65 (± 0.12)	37.18 (± 0.22)	< −4–13 >	< 1–21 >	< 234 >
#7	355.16 (± 1.03)	10.14 (± 0.19)	23.14 (± 1.05)	< 3–10 >	< 14–1 >	< 014 >
#8	126.80 (± 0.25)	27.20 (± 0.14)	85.42 (± 0.24)	< −432 >	< −2–41 >	< 102 >
#9	34.87 (± 0.26)	28.03 (± 0.34)	31.24 (± 0.17)	< 2–41 >	< 31–1 >	< 124 >

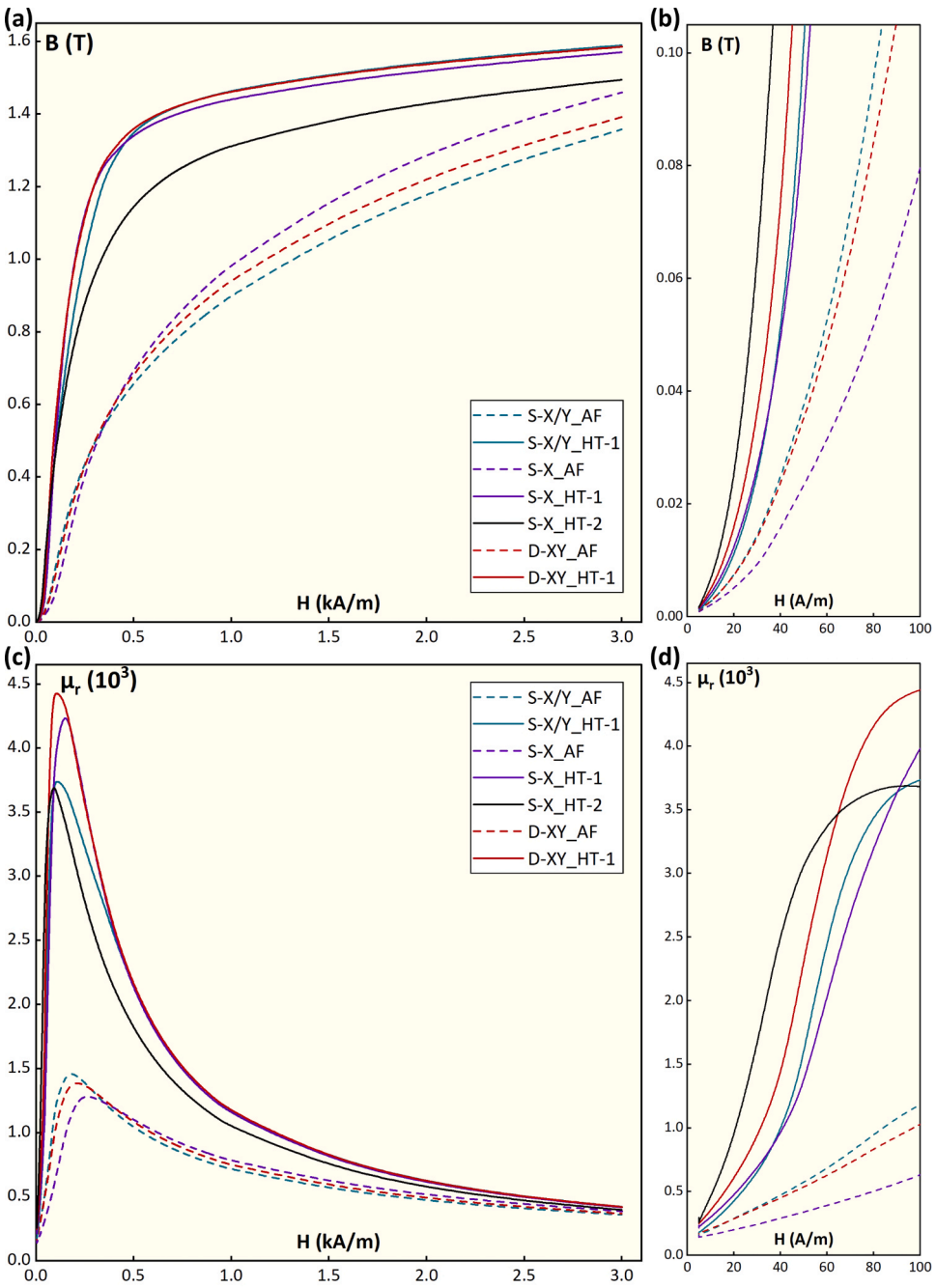

Fig. 9. (a) and (c) are quasi-static magnetization curves and corresponding μ_r, respectively. (b) and (d) are magnified versions of H = 0–100A/m in (a) and (c), respectively.

4. Discussion

4.1. Formation of texture under different scanning strategies

To clarify the formation mechanism of texture components, the morphology of MP in YZ-, XZ-, and XY-plane was investigated and presented in Fig. 12, Fig. S2, and Fig. 13, respectively.

4.1.1. Formation of out-of-plane texture

In Fig. 12 and Fig.S2, the dashed lines represent molten pool boundaries (MPB), and the directions of epitaxial growth are approximately illustrated by the arrows. As < 001 > is the preferred solidification crystal orientation in BCC structures, these arrows also signify the direction of the < 001 > crystal orientation. Besides, IPF-Z colored EBSD maps in XZ- and YZ-plane are also provided in Fig. S3, in which the well-developed epitaxial grain growth can be demonstrated from the columnar grains exceeding dozens of layers exhibiting the same grain orientations with respect to BD. The formation of different texture types at the shell and the core of the samples can be explained by two characteristics of the side morphology of MP, which are (i) the lack or absence of remelting in the first and last scanning tracks of each layer in Fig. 12 (a), and (ii) the heat concentration induced deeper MP at the head/tail of the scanning track in Fig. 2 (b).

As illustrated by the dashed lines in Fig. 12 (a4) and Fig. S2 (b2), a single scanning track exhibited a keyhole shape with the laser penetrating much deeper than its affecting width. As the direction of the epitaxial grain growth is essentially perpendicular to the MPB [67], only the bottom region of the keyhole-shaped MP enabled the grains to grow

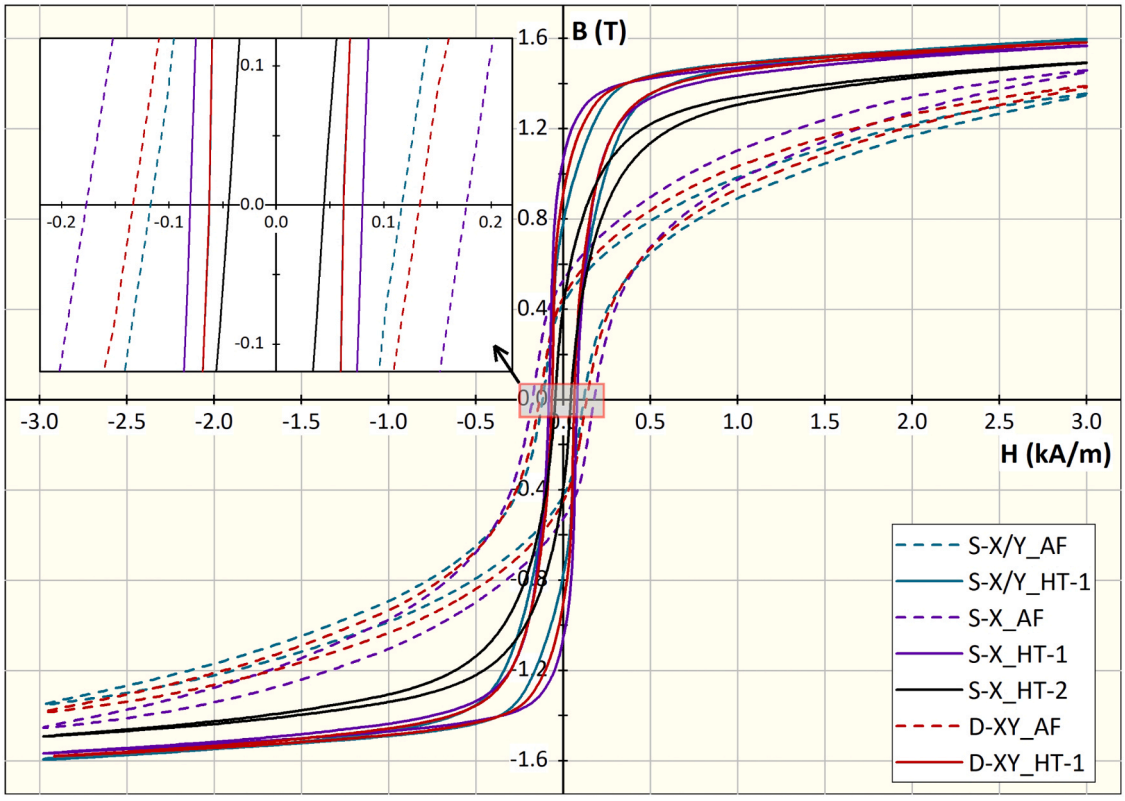

Fig. 10. Quasi-static B-H hysteresis loop.

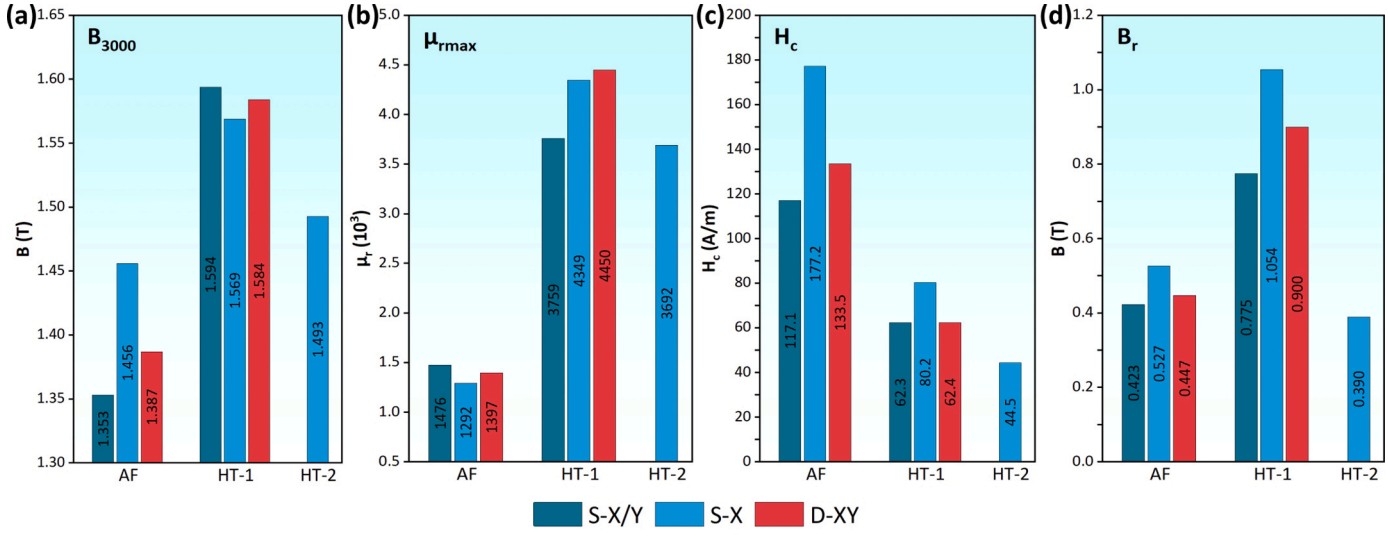

Fig. 11. The comparison of B_{3000}, μ_{rmax}, H_c, and B_r of AF and HTed samples.

Table 2
The statistics of the quasi-static magnetic properties in Fig. 10 and Fig. 11 with a comparison to other work.

Materials	Fabrication	Condition	B_{3000} (T)	μ_{rmax}	μ_i (mH/m)	H_c (A/m)	B_r (T)	Ref.
Fe−3.5 wt%Si	S-X/Y	AF	1.353	1476	0.2093	117.1	0.423	This work
	S-X	AF	1.456	1292	0.1850	177.2	0.527	
	D-XY	AF	1.387	1397	0.2198	133.5	0.447	
	S-X/Y	HT−1	1.594	3759	0.2258	62.3	0.775	
	S-X	HT−1	1.569	4349	0.2820	80.2	1.054	
	D-XY	HT−1	1.584	4450	0.3164	62.4	0.900	
	S-X	HT−2	1.493	3692	0.3383	44.5	0.390	
Fe−3 wt%Si	LPBF	HTed	1.641 (B_{5000})	3370	N.A.	92	0.763	[66]

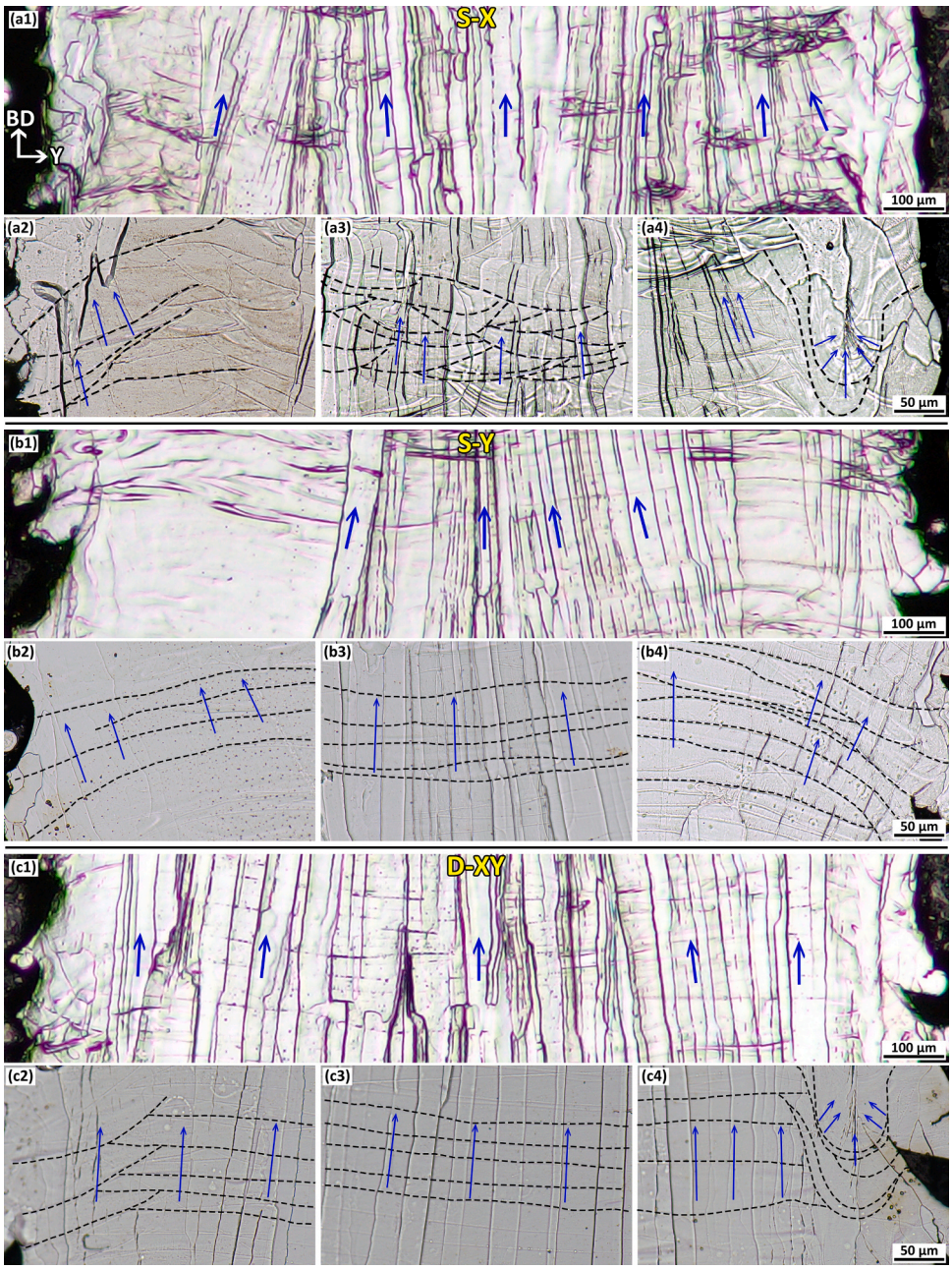

Fig. 12. The side morphology of MP in YZ-plane. (a)-(c) represent S-X, S-Y, and D-XY, respectively, and (2)-(4) are the magnified versions from the left-side boundary, center, and right-side boundary of the entire width of the samples (i.e., (1)), respectively. The dashed lines and blue arrows show the MPB and epitaxial growth direction, respectively.

parallel to BD, forming the < 001 > //BD texture, while the grains in the upper region tended to grow at various angles with respect to BD under the additional affected by Marangoni flow. This was also observed in the LPBF-manufactured FeCrAl alloy by Dovgyy et al., where only the grains located in the center of the MP can outgrow grains from the side of MP to across multiple layers with a preferred orientation of < 001 > //BD, making them highly textured and columnar [68]. Therefore, the grain orientations with respect to BD varied along the depth direction of the MP within a single track rather than forming a uniformly < 001 > //BD texture. To finally form the strong < 001 > //BD texture in Fig. 2, the remelting of the MP by the following scanning played a crucial role. The different morphology of MP in Fig. 12 (a3) and Fig. S2 (b1) (the core of the samples) from Fig. 12 (a4) and Fig. S2 (b2) suggests that the remelting from the adjacent tracks not only enlarged and flattened the bottom region of the MP but also removed the side part of the MP, which enhanced the strength of the < 001 > //BD texture and eliminated non-< 001 > //BD grains, respectively. When the successive layers were added, the non-< 001 > //BD grains in the upper region of the MP were also removed by the remelting effect from these layers. Ultimately, only the bottom region of the MP with < 001 > //BD grains remained leading to the formation of a strong < 001 > //BD texture. However, for the first (Fig. 12 (a2)) and the last scanning tracks (Fig. 12 (a4)) in each layer, the remelting process by the adjacent tracks was insufficient or even absent, respectively, resulting in the curved MPB. Since the curved MPB was not conducive for grains to grow with < 001 > //BD, the non-< 001 > //BD grains were observed at the shell of the S-X sample in Fig. 2 (b).

The morphology of MP in Fig. 12 (b) suggests that the heat concentration at the head/tail of the scanning track was another factor causing the formation of non-< 001 > //BD grains at the shell of the

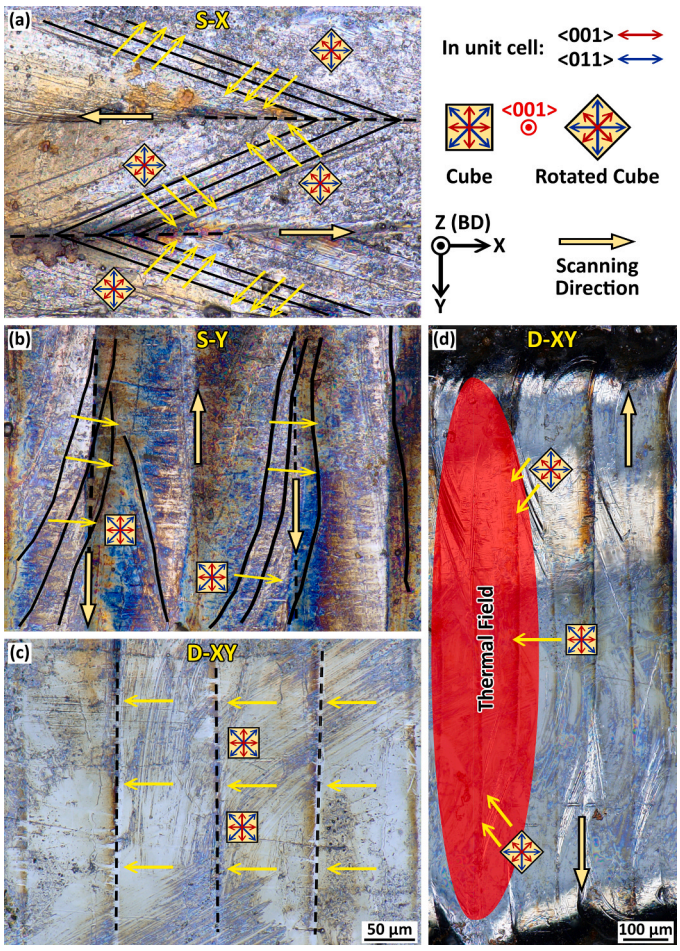

Fig. 13. (a)-(c) are the top surfaces of S-X, S-Y, and D-XY, respectively, and (d) is the entire width version of D-XY. The solid lines, dash lines, and yellow arrows represent the MPB, center lines of laser movement, and approximate thermal gradient, respectively.

sample. In the center of the scanning tracks, the continuous movement of the laser and sufficient cooling time were beneficial for forming a stable and uniform thermal field. However, at the head/tail of the scanning tracks in the unconnected zigzag scanning pattern, the short interval for cooling and the high energy input from the starting laser pulse of each scanning resulted in an unstable MP with heat concentration. Thus, the MPB appeared relatively straight and flat at the center of the scanning tracks (Fig. 12 (b3)), but drooped at the head/tail of the scanning tracks (Fig. 12 (b2, b4)). As indicated by the blue arrows in Fig. 12 (b), the former scenario was beneficial for grains to grow epitaxially along the BD, while the latter scenario led to a deviation of the directions of epitaxial growth of grains from the BD. Therefore, $< 001 >$//BD and non-$< 001 >$//BD grains appeared at the shell and the core of the S-Y sample, respectively.

According to Fig. 12 (c) and Fig. S2 (c), the enhancement of the θ-fiber texture in the D-XY sample can be inferred as the result of the more regular MP formed during the second scanning pass. On one hand, the MP in Fig. 12 (c) and Fig. S2 (c), exhibited similar characteristics to the S-X samples and S-Y samples at the shell (lack or absence of remelting) and the core (straight and flat MPB) regions, respectively. On the other hand, the MP in Fig. 12 (c) showed a much more regular pattern with the almost parallel MPB. This refinement in the MP morphology of the D-XY sample may be due to the more uniform and stable thermal field during the second scanning pass. In comparison to the powder bed in the first scanning pass, the solidified bulk bed with a smoother surface in the second scanning pass had a smaller specific surface area and higher laser reflectivity, which can efficiently reduce the energy absorption of the laser beam by the printed materials. Benefiting from this reduced energy absorption, when the second scanning pass of the D-XY sample moved along the same route as S-Y, the heat concentration, which happened in the S-Y sample, was effectively relieved, and the deeper MP was thus avoided. As a result, the straight and flat MPB in the core of the sample was even retained in the shell region of D-XY samples (Fig. 12 (c2, c4)), which significantly eliminated the strong $< 111 >$//BD texture at the shell of the S-Y sample. Consequently, with the benefits of the refined MP morphology, epitaxial growth was significantly promoted to align with BD in the D-XY samples, even in the shell region, ultimately leading to the enhancement of the θ-fiber texture in the D-XY sample.

Except above two characteristics of the side morphology of MP, the aspect ratio of columnar grains was also reported as the factor influencing grain orientations with respect to BD. Specifically, an aspect ratio greater than 4 promotes the formation of $< 001 >$//BD texture, while an aspect ratio below 4 tends to result in little texture development [68]. According to Fig. S3, the aspect ratio of nearly all columnar grains clearly exceeds 4, suggesting that this factor is likely not the primary reason for the formation of different texture types in this study.

4.1.2. *Formation of in-plane texture*

In Fig. 13, the solid lines, dashed lines, and yellow arrows represent the MPB, laser movement route (i.e., scanning track center), and the approximate thermal gradient directions, respectively. In the following discussion about the formation mechanism of in-plane texture, only the θ-fiber texture will be taken into consideration due to its dominance in the texture components in this research.

Similar to the findings in our previous study [37], the MP in the S-X samples exhibited a teardrop shape, a result of the combination of high laser power and fast scanning speed, which can be characterized by straight and sharp MPB tails. Since the thermal gradient is essentially nearly perpendicular to the MPB (as indicated by the yellow arrows in Fig. 13 (a)), the direction of the grain growth, which is also the $< 001 >$ crystal orientation in BCC, would also approximate be perpendicular to the MPB. Considering the geometric relationship between $< 001 >$ and $< 011 >$ (represented by the yellow cube in Fig. 13), the $< 011 >$ crystal orientation pointed to the SD (i.e., X-axis). The combination of $< 011 >$//X-axis and $< 001 >$//BD ultimately enabled a strong Rotated Cube texture formed in the S-X samples.

In S-Y samples, the short length of the scanning tracks led to shorter intervals between adjacent scanning tracks as compared to the S-X samples. As a result, although the laser scanned along the Y-axis in the S-Y samples, the overall thermal field was generally distributed along the X-axis with the thermal gradients in a similar direction. As evidence, the MPB in Fig. 13 (b) even crossed the center of the scanning track. This finding was also confirmed by Haines et al. with the simulation of the thermal field of the short scanning tracks (0.5 mm) [48]. This feature of the thermal field enabled the grains to grow with their $< 001 >$ crystal orientations along the X-axis, forming a Cube texture in the S-Y samples. However, since most grains in the S-Y samples oriented with non-$< 001 >$//BD, only limited grains at the core of the samples finally exhibited Cube texture.

Similar to the previous analysis of the side morphology of MP, the top morphology of MP was also refined due to the more uniform and stable thermal field during the second scanning pass. The above thermal field feature in the S-Y samples was enhanced by the refined MP, where except for the centerline of the scanning track, no other fusion lines are observed at the center of the sample in Fig. 13 (c). The absence of fusion lines further also demonstrated that the overall thermal field was distributed along the X-axis, as illustrated by the red region in Fig. 13 (d). As the preferred solidification direction is essentially parallel to the thermal gradient, it can be inferred from the schematic of this thermal field and the observed fusion lines at the shell of the samples in Fig. 13 (d) that the grains most possibly solidified with their $< 011 >$//X-axis

and < 001 > //X-axis at the shell and core of the D-XY samples, respectively, which is well matched with IPF-X color pattern in Fig. 2 (d2). Finally, taking advantage of the enhanced < 001 > //BD grains by the second scanning pass, the strong Cube texture was formed in the D-XY samples.

4.2. Relationship between microstructure and quasi-static magnetic properties

In this study, the quasi-static magnetic properties were influenced by three microstructural factors: (i) the residual stress and dislocation density, (ii) the texture components, and (iii) the grain size.

Since the texture components and the grain size of AF samples were not changed after HT-1 annealing, the improvement of the quasi-static magnetic properties of HT-1 samples mainly resulted from the relief of the residual stress and reduction of the dislocation density by the recovery. In AF samples, the existence of high residual stress and the dislocations could cause lattice distortion, which increased magnetic anisotropy and reduced the permeability. Besides, the dislocations themselves also acted as obstructions hindering the domain wall displacement during the magnetization process. Therefore, the AF samples exhibited a much harder magnetic response, and the μ_r was increased significantly after annealing.

After HT, it could be considered as that the residual stress was fully relieved, and the dislocation densities were reduced to a similar level. The texture components and grain size then became the primary factors affecting quasi-static magnetic properties, and the details of the grain sizes of the HT samples are provided in Fig. 14. In general, the stronger < 001 > //H texture and the larger grain size are beneficial for achieving a softer magnetic behavior due to lower required magnetization work, but their effect on the quasi-static magnetic characteristics differed at the different magnetization stages. When the samples were magnetized under a weak H (i.e., H ~< 50 A/m), the magnetization process occurred only in the manner of the domain wall displacement, which can be hindered by domain wall pinning from the grain boundaries. Therefore, the HT-2 S-X sample, which took great advantage of its large grain size (66.8 μm) induced by AGG, exhibited the softest magnetic response (i.e., the highest μ_r) at this stage, even though the grain orientations of the AGG grains were random instead of the preferred one (as in the HT-1 D-XY samples). As H increased, the magnetization mechanism of the samples gradually changed to the rotation of the magnetization vector ($\vec{M}$), so differences in magnetocrystalline anisotropy of different texture components started to affect the magnetization hardness. Specifically, the strong < 001 > //H texture in the HT-1 D-XY sample made its retained $\vec{M}$ closer to the direction of H than other HT samples, so less magnetization work was required for it to rotate $\vec{M}$

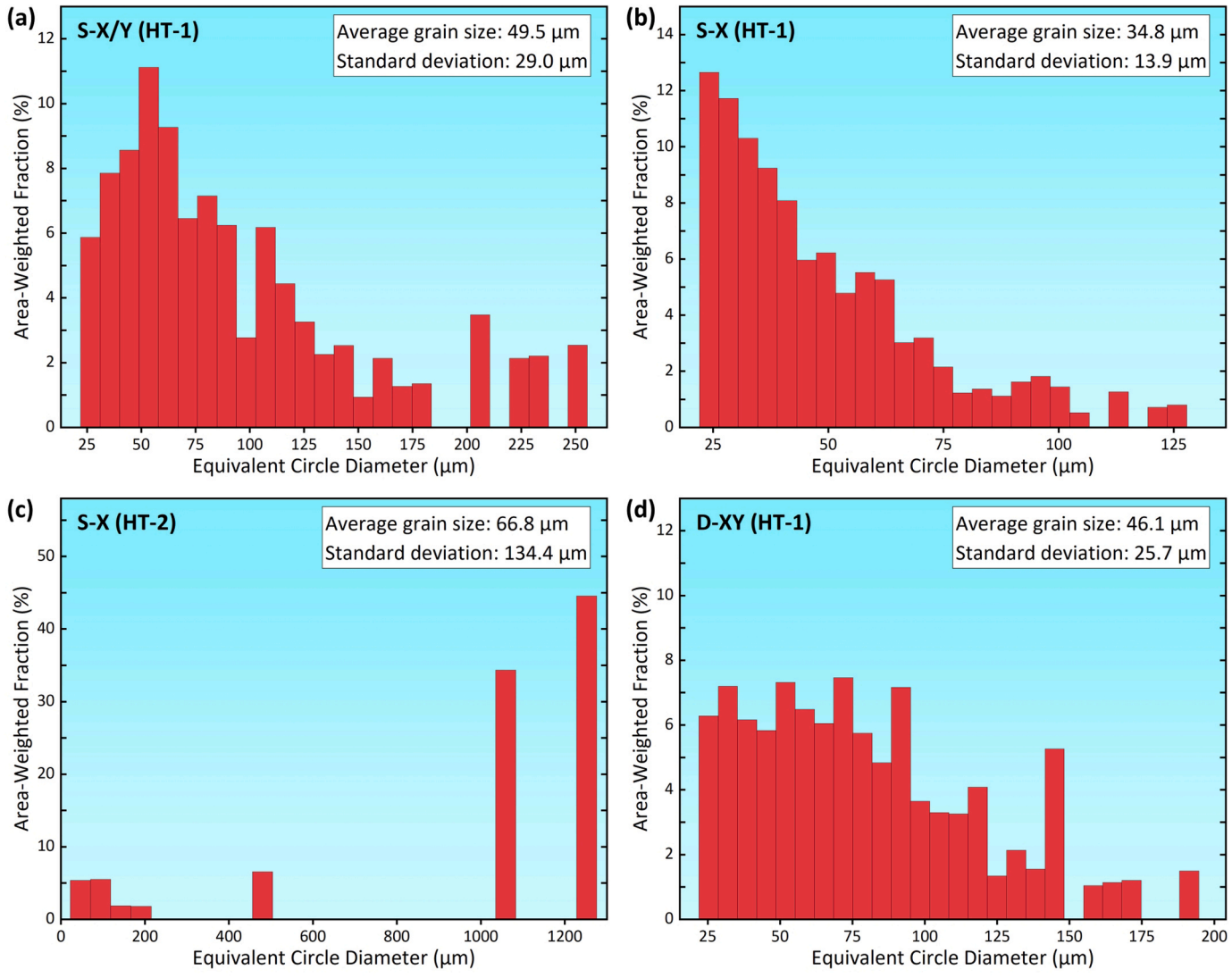

Fig. 14. The grain sizes of the HTed samples.

pointing to the direction of H. Therefore, the HT-1 D-XY sample with the extremely strong {100}< 001 > crystallographic texture and larger grain size (46.1 μm) achieved the softest magnetic response at this stage, characterized by its excellent μ_r and the highest μ_{rmax}. In contrast, the HT-2 S-X sample became the most difficult one to be magnetized due to the highest magnetization work required to rotate $\vec{M}$ in the AGG grains with random crystallographic orientations pointing to the direction of H. Similar to [69], the same magnetization behavior has been seen in conventional manufactured soft magnetic materials in different magnetization regions.

The effect of above microstructure characteristics on H_c can be discussed by the GSDCP theory, in which H_c is described as a function of average grain size (D). Specifically, when the grain size is larger than the domain wall width, this function could be expressed as [70]:

$$H_C \approx 3\sqrt{\frac{k_B T_c K_1}{\alpha J_s}}\ \frac{1}{D} \tag{1}$$

Where k_B is the Boltzmann constant, T_c is Curie Temperature, K_1 is magnetocrystalline anisotropy, α is lattice constant, and J_s is magnetic saturation polarization. In Eq. 1, the influence of microstructure features other than grain size (such as residual stress, lattice defects, lattice distortion, and disordering structure, etc.) on the H_c is reflected on affecting K_1 and α, which is why the H_c of the AF samples was significantly higher than that of the HT-1 samples, even though there was no grain growth during HT-1., The H_c and D^{-1} of all the measured samples in this study were summarized in Fig. 15 for further exploration of their relationship. Since the residual stress and lattice distortion have been relieved by annealing and Fe-3.5Si (wt%) is a single-phase structure, the K_1 and α can be assumed as constants in the HT samples. Taking T_c = 1043 K, $K_1 = 34 \times 10^3$ J/m^3, α = 2.86 Å, and J_s = 2 T [5,7,71,72] into Eq. 1, the expression becomes:

$$H_c = 2776.2 \times D^{-1} \tag{2}$$

Meanwhile, the relationship between H_c and D^{-1} of the HT samples in this study was also fitted with a linear function, which the expression is:

$$H_c = 7.94 + 2542.4 \times D^{-1} \tag{3}$$

Eq. 2 and Eq. 3 were plotted as dashed and solid lines in Fig. 15, respectively. It could be found that the fitted expression is well matched with the theoretically calculated expression in Fig. 15. This not only confirms the relief of residual stress through annealing but also suggests that texture components do not significantly affect H_c. Moreover, it provides valuable insights into the numerical relationship between grain size and H_c in this research.

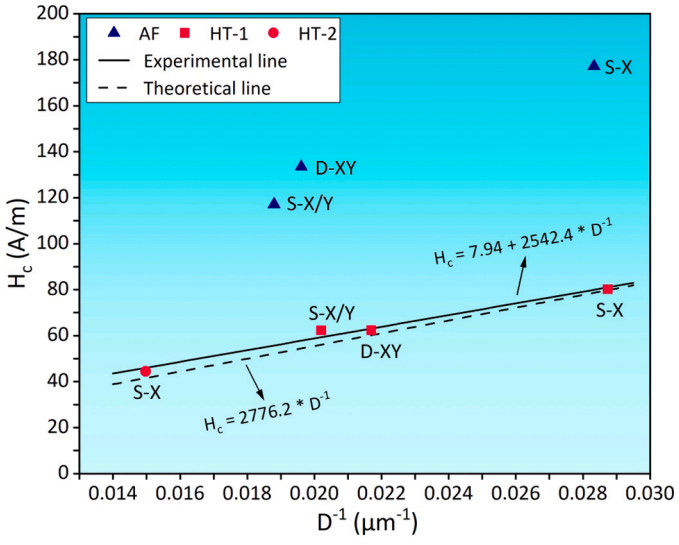

Fig. 15. Comparison of H_c vs D^{-1} obtained in this study.

4.3. *Proposed method to control in-plane grain orientation distribution of LPBFed electrical steels*

According to the findings in this research, a method to control in-plane grain orientation distribution of Fe-3.5Si (wt%) of a certain shape can be proposed. The basic idea is illustrated in Fig. 16 as the example. The long scanning along the contour shape of the object (shown as blue arrow lines) would enable the < 011 > crystal orientation to align with the contour shape. Subsequently, performing another short scanning perpendicular to the initial scan (shown as red arrow lines) in the same layer can replace this < 011 > crystal orientation with < 001 > crystal orientation.

5. Conclusions

In this research, the laser powder bed fusion (LPBF)-manufactured Fe-3.5Si (wt%) with extremely strong Rotated Cube texture (i.e., {001}<011 >) and Cube texture (i.e., {001}<001 >) was obtained by using scanning strategy (SS) of the single scanning along X-axis (denoted as S-X) and double scanning along X-axis and Y-axis successively in the same layer (denoted as D-XY), respectively. A comprehensive characterization and comparison of the quasi-static magnetic properties of as-fabricated (AF) and heat-treated (HTed) samples was conducted using DC closed magnetic circuit testing. Furthermore, the formation mechanism of texture and microstructural effects on quasi-static magnetic properties were investigated. The key findings of this study can be summarized as follows:

(1) Regarding the out-of-plane texture, the sufficient remelting and the uniform and stable thermal field in molten pools (MP) located at the core of samples facilitated the formation of a strong θ-fiber texture by promoting epitaxial growth aligned with building directions (BD). However, the epitaxial growth at the shell of the samples deviated from BD due to the lack or absence of remelting and deeper MP induced by heat concentration, which led to the formation of non-< 001 > //BD grains.

(2) As the scanning track length decreased, the in-plane grain orientations of θ-fiber texture shifted from < 011 > //X-axis to < 001 > //X-axis due to the different cooling conditions. The sufficient cooling time of MP in a long scanning track enabled to form a teardrop-shaped thermal field, while the heat concentration due to the shorter intervals between shorter tracks led to the formation of a larger elliptical thermal field across the entire width of the samples. The distinct thermal gradients in these two thermal fields resulted in grains at the core of the samples growing with < 011 > //X-axis and < 001 > //X-axis in the long and short scanning tracks, respectively.

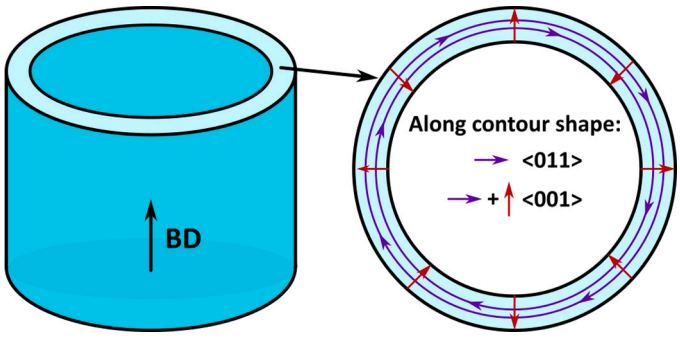

Fig. 16. Illustration for the proposed method of controlling grain orientations.

(3) In the D-XY samples, the morphology of MP can be refined by the more uniform and stable thermal field in the second scanning pass. This refinement of the MP enhanced the characteristics beneficial for the formation of both $< 001 >$//BD and $< 001 >$//X-axis grains, ultimately developing into a strong Cube texture.
(4) The grain size and the texture components in the HTed S-X/Y and HTed D-XY samples retained the same as the AF condition. In this research, grain growth only occurred in the manner of abnormal grain growth (AGG) and was observed only in the S-X samples under specific heat treatment (HT) conditions. All the HT conditions used in this research cannot promote AGG grains to consume all the matrix grains to obtain the microstructure with the entirely AGG grains.
(5) Quasi-static magnetic properties of AF samples were deteriorated seriously by the residual stress and dislocations, which can be eliminated by HT. When the samples were magnetized through domain wall displacement (magnetic field strength (H) $\sim<$ 50 A/m) and rotation of the magnetization vector (H $\sim>$50 A/m), the magnetic response could be softened by the large grain size and the desirable texture component (i.e., $<001>$//H), respectively. According to Grain Size Dependence of Coercivity and Permeability (GSDCP) theory, the large grain size can also reduce the coercivity (H_c). Benefitting from the corresponding microstructural advantages, the D-XY sample annealed at 1000℃ for 2 hours (HT-1) exhibited the excellent overall relative permeability (μ_r) and highest maximum relative permeability (μ_{rmax}) of 4450, and the S-X samples annealed at 1150℃ for 4 hours (HT-2) achieved highest μ_r at H $\sim<$ 50 A/m and lowest H_c of 44.5 A/m.

Finally, a method to control the in-plane grain orientation distribution of Fe-3.5Si (wt%) of a certain shape was proposed. Based on this method, it will be possible to control the $< 001 >$ or $< 011 >$ crystal orientations distributing along the wanted direction in the electric motor with a certain geometry by designing SS, hence providing potential methods to improve motor performances.

CRediT authorship contribution statement

Fanbo Meng: Writing – original draft, Validation, Methodology, Investigation, Formal analysis, Conceptualization. **Christopher H. T. Lee:** Writing – review & editing, Supervision, Funding acquisition. **Xiaojun Shen:** Writing – review & editing. **Pei Wang:** Writing – review & editing. **Alexander M. Korsunsky:** Writing – review & editing. **Yuheng Deng:** Investigation. **Kwang Boon Lau:** Investigation. **Konstantinos A. Liogas:** Writing – review & editing, Formal analysis.

Declaration of Competing Interest

The authors declare that they have no known competing financial interests or personal relationships that could have appeared to influence the work reported in this paper.

Acknowledgments

The research of the project is supported by the Panasonic Industrial Devices Singapore Pte. Ltd, Singapore, under its Joint Lab Programme 04IDS001408C140. This research is supported by A*STAR under its RIE2025 MTC IAF-PP: Development of High Performance Electric Traction Module, Grant No. M22K4a0044. We also would like to acknowledge the Facility for Analysis, Characterisation, Testing and Simulation, Nanyang Technological University, Singapore, for use of their electron microscopy.

Appendix A. Supporting information

Supplementary data associated with this article can be found in the online version at doi:10.1016/j.addma.2024.104614.

Data availability

Data will be made available on request.

References

[1] A. Krings, A. Boglietti, A. Cavagnino, S. Sprague, Soft magnetic material status and trends in electric machines, IEEE Trans. Ind. Electron. 64 (2017) 2405–2414, https://doi.org/10.1109/TIE.2016.2613844.
[2] G. Ouyang, X. Chen, Y. Liang, C. Macziewski, J. Cui, Review of Fe-6.5 wt%Si high silicon steel—a promising soft magnetic material for sub-kHz application, J. Magn. Magn. Mater. 481 (2019) 234–250, https://doi.org/10.1016/j.jmmm.2019.02.089.
[3] T.N. Lamichhane, L. Sethuraman, A. Dalagan, H. Wang, J. Keller, M. P. Paranthaman, Additive manufacturing of soft magnets for electrical machines—a review, Mater. Today Phys. 15 (2020) 100255, https://doi.org/10.1016/j.mtphys.2020.100255.
[4] V. Chaudhary, S.A. Mantri, R.V. Ramanujan, R. Banerjee, Additive manufacturing of magnetic materials, Prog. Mater. Sci. 114 (2020) 100688, https://doi.org/10.1016/j.pmatsci.2020.100688.
[5] M.E. McHenry, D.E. Laughlin, Magnetic properties of metals and alloys. in: Physical Metallurgy, Elsevier, 2014, pp. 1881–2008, https://doi.org/10.1016/B978-0-444-53770-6.00019-8.
[6] J.M. Silveyra, E. Ferrara, D.L. Huber, T.C. Monson, Soft magnetic materials for a sustainable and electrified world, Science 362 (2018) eaao0195, https://doi.org/10.1126/science.aao0195.
[7] G.E. Fish, Soft magnetic materials, Proc. IEEE 78 (1990) 947–972, https://doi.org/10.1109/5.56909.
[8] R. Wrobel, B. Mecrow, A comprehensive review of additive manufacturing in construction of electrical machines, IEEE Trans. Energy Convers. 35 (2020) 1054–1064, https://doi.org/10.1109/TEC.2020.2964942.
[9] T. Pham, P. Kwon, S. Foster, Additive manufacturing and topology optimization of magnetic materials for electrical machines—a review, Energies 14 (2021) 283, https://doi.org/10.3390/en14020283.
[10] S. Madichetty, S. Mishra, M. Basu, New trends in electric motors and selection for electric vehicle propulsion systems, IET Electr. Syst. Transp. 11 (2021) 186–199, https://doi.org/10.1049/els2.12018.
[11] F. Wu, A.M. EL-Refaie, Toward additively manufactured electrical machines: opportunities and challenges, IEEE Trans. Ind. Appl. 56 (2020) 1306–1320, https://doi.org/10.1109/TIA.2019.2960250.
[12] Y. Zhou, J. Liu, F. Meng, G. Yang, Y. He, D.K.B. Lau, P. Wang, C.H.T. Lee, Design of an Axial-Flux Synchronous Reluctance Machine with 3D-Printed Rotor, in: 2023 IEEE International Electric Machines & Drives Conference (IEMDC), IEEE, San Francisco, CA, USA, 2023: pp. 1–7. https://doi.org/10.1109/IEMDC55163.2023.10238945.
[13] G. Herzer, Grain size dependence of coercivity and permeability in nanocrystalline ferromagnets, IEEE Trans. Magn. 26 (1990) 1397–1402, https://doi.org/10.1109/20.104389.
[14] G. Herzer, Grain structure and magnetism of nanocrystalline ferromagnets, IEEE Trans. Magn. 25 (1989) 3327–3329, https://doi.org/10.1109/20.42292.
[15] G. Herzer, Soft magnetic nanocrystalline materials, Scr. Metall. Et. Mater. 33 (1995) 1741–1756, https://doi.org/10.1016/0956-716X(95)00397-E.
[16] G. Herzer, Anisotropies in soft magnetic nanocrystalline alloys, J. Magn. Magn. Mater. 294 (2005) 99–106, https://doi.org/10.1016/j.jmmm.2005.03.020.
[17] D. Xue, G. Chai, X. Li, X. Fan, Effects of grain size distribution on coercivity and permeability of ferromagnets, J. Magn. Magn. Mater. 320 (2008) 1541–1543, https://doi.org/10.1016/j.jmmm.2008.01.004.
[18] D. Dorner, S. Zaefferer, L. Lahn, D. Raabe, Overview of microstructure and microtexture development in grain-oriented silicon steel, J. Magn. Magn. Mater. 304 (2006) 183–186, https://doi.org/10.1016/j.jmmm.2006.02.116.
[19] H. Liu, Z. Liu, G. Cao, C. Li, G. Wang, Microstructure and texture evolution of strip casting 3wt% Si non-oriented silicon steel with columnar structure, J. Magn. Magn. Mater. 323 (2011) 2648–2651, https://doi.org/10.1016/j.jmmm.2011.06.002.
[20] Y.H. Sha, C. Sun, F. Zhang, D. Patel, X. Chen, S.R. Kalidindi, L. Zuo, Strong cube recrystallization texture in silicon steel by twin-roll casting process, Acta Mater. 76 (2014) 106–117, https://doi.org/10.1016/j.actamat.2014.05.020.
[21] R. Liang, P. Yang, W. Mao, Retaining {1 0 0} texture from initial columnar grains in 6.5 wt% Si electrical steels, J. Magn. Magn. Mater. 441 (2017) 511–516, https://doi.org/10.1016/j.jmmm.2017.05.092.
[22] H.-Y. Song, H.-T. Liu, H.-H. Lu, H.-Z. Li, W.-Q. Liu, X.-M. Zhang, G.-D. Wang, Effect of hot rolling reduction on microstructure, texture and ductility of strip-cast grain-oriented silicon steel with different solidification structures, Mater. Sci. Eng.: A 605 (2014) 260–269, https://doi.org/10.1016/j.msea.2014.03.052.
[23] H. Jiao, Y. Xu, L. Zhao, R.D.K. Misra, Y. Tang, D. Liu, Y. Hu, M. Zhao, M. Shen, Texture evolution in twin-roll strip cast non-oriented electrical steel with strong Cube and Goss texture, Acta Mater. 199 (2020) 311–325, https://doi.org/10.1016/j.actamat.2020.08.048.

[24] J.Y. Park, K.S. Han, J.S. Woo, S.K. Chang, N. Rajmohan, J.A. Szpunar, Influence of primary annealing condition on texture development in grain oriented electrical steels, Acta Mater. 50 (2002) 1825–1834, https://doi.org/10.1016/S1359-6454(02)00034-4.

[25] A. Morawiec, Grain misorientations in theories of abnormal grain growth in silicon steel, Scr. Mater. 43 (2000) 275–278, https://doi.org/10.1016/S1359-6462(00)00403-6.

[26] N. Maazi, N. Rouag, A.L. Etter, R. Penelle, T. Baudin, Influence of neighbourhood on abnormal Goss grain growth in Fe–3% Si steels: formation of island grains in the large growing grain, Scr. Mater. 55 (2006) 641–644, https://doi.org/10.1016/j.scriptamat.2006.06.007.

[27] T. Omori, T. Kusama, S. Kawata, I. Ohnuma, Y. Sutou, Y. Araki, K. Ishida, R. Kainuma, Abnormal grain growth induced by cyclic heat treatment, Science 341 (2013) 1500–1502, https://doi.org/10.1126/science.1238017.

[28] A. Morawiec, On abnormal growth of Goss grains in grain-oriented silicon steel, Scr. Mater. 64 (2011) 466–469, https://doi.org/10.1016/j.scriptamat.2010.11.013.

[29] K. Jenkins, M. Lindenmo, Precipitates in electrical steels, J. Magn. Magn. Mater. 320 (2008) 2423–2429, https://doi.org/10.1016/j.jmmm.2008.03.062.

[30] K.-J. Ko, A.D. Rollett, N.-M. Hwang, Abnormal grain growth of Goss grains in Fe–3% Si steel driven by sub-boundary-enhanced solid-state wetting: analysis by Monte Carlo simulation, Acta Mater. 58 (2010) 4414–4423, https://doi.org/10.1016/j.actamat.2010.04.038.

[31] A. Rollett, On the growth of abnormal grains, Scr. Mater. 36 (1997) 975–980, https://doi.org/10.1016/S1359-6462(96)00501-5.

[32] N. Chen, S. Zaefferer, L. Lahn, K. Günther, D. Raabe, Effects of topology on abnormal grain growth in silicon steel, Acta Mater. 51 (2003) 1755–1765, https://doi.org/10.1016/S1359-6454(02)00574-8.

[33] M. Hillert, On the theory of normal and abnormal grain growth, Acta Metall. 13 (1965) 227–238, https://doi.org/10.1016/0001-6160(65)90200-2.

[34] P.R. Rios, Abnormal grain growth development from uniform grain size distributions, Acta Mater. 45 (1997) 1785–1789, https://doi.org/10.1016/S1359-6454(96)00284-4.

[35] S. Birosca, A. Nadoum, D. Hawezy, F. Robinson, W. Kockelmann, Mechanistic approach of Goss abnormal grain growth in electrical steel: theory and argument, Acta Mater. 185 (2020) 370–381, https://doi.org/10.1016/j.actamat.2019.12.023.

[36] X. Shen, F. Meng, K.B. Lau, P. Wang, C.H.T. Lee, Texture and microstructure characterizations of Fe-3.5wt%Si soft magnetic alloy fabricated via laser powder bed fusion, Mater. Charact. 189 (2022) 112012, https://doi.org/10.1016/j.matchar.2022.112012.

[37] F. Meng, S. Huang, K.B. Lau, Y. Zhou, Y. Deng, P. Wang, X. Shen, C.H.T. Lee, Texture components and magnetic properties of laser powder bed fusion fabricated near grain-oriented and near non-oriented silicon steel, Mater. Des. 231 (2023) 112037, https://doi.org/10.1016/j.matdes.2023.112037.

[38] A.Z. Macknojia, J.V. Tran, M.P. McKinstry, J. Galindo, Y. Jin, S. Dowden, S. M. Patil, M.V. Pantawane, K.V.M. Krishna, R. Banerjee, S.S. Joshi, N.B. Dahotre, Additive manufacturing of Fe-6.5 wt%Si transformer steel toroidal cores: process optimization, design aspects, and performance, Mater. Des. 241 (2024) 112883, https://doi.org/10.1016/j.matdes.2024.112883.

[39] M. Garibaldi, I. Ashcroft, M. Simonelli, R. Hague, Metallurgy of high-silicon steel parts produced using selective laser melting, Acta Mater. 110 (2016) 207–216, https://doi.org/10.1016/j.actamat.2016.03.037.

[40] M. Garibaldi, I. Ashcroft, N. Hillier, S.A.C. Harmon, R. Hague, Relationship between laser energy input, microstructures and magnetic properties of selective laser melted Fe-6.9%wt Si soft magnets, Mater. Charact. 143 (2018) 144–151, https://doi.org/10.1016/j.matchar.2018.01.016.

[41] M. Garibaldi, I. Ashcroft, J.N. Lemke, M. Simonelli, R. Hague, Effect of annealing on the microstructure and magnetic properties of soft magnetic Fe-Si produced via laser additive manufacturing, Scr. Mater. 142 (2018) 121–125, https://doi.org/10.1016/j.scriptamat.2017.08.042.

[42] G. Stornelli, A. Faba, A. Di Schino, P. Folgarait, M.R. Ridolfi, E. Cardelli, R. Montanari, Properties of additively manufactured electric steel powder cores with increased Si content, Materials 14 (2021) 1489, https://doi.org/10.3390/ma14061489.

[43] F. Galbusera, L. Caprio, B. Previtali, A.G. Demir, Tailoring the microstructure of Fe-2.9wt%Si alloy in laser powder bed fusion using in-source beam shaping, Opt. Laser Technol. 174 (2024) 110649, https://doi.org/10.1016/j.optlastec.2024.110649.

[44] M. Ahmadnia, E. Fereiduni, M. Yakout, M. Elbestawi, R.K. R M, G. Vakil, R. Muizelaar, Optimizing magnetic performance of Fe–50Ni alloy for electric motor cores through LPBF: a study of as-built and heat-treated scenarios, J. Mater. Res. Technol. 29 (2024) 2554–2571, https://doi.org/10.1016/j.jmrt.2024.02.011.

[45] N. Nadammal, T. Mishurova, T. Fritsch, I. Serrano-Munoz, A. Kromm, C. Haberland, P.D. Portella, G. Bruno, Critical role of scan strategies on the development of microstructure, texture, and residual stresses during laser powder bed fusion additive manufacturing, Addit. Manuf. 38 (2021) 101792, https://doi.org/10.1016/j.addma.2020.101792.

[46] J.J. Marattukalam, D. Karlsson, V. Pacheco, P. Beran, U. Wiklund, U. Jansson, B. Hjörvarsson, M. Sahlberg, The effect of laser scanning strategies on texture, mechanical properties, and site-specific grain orientation in selective laser melted 316L SS, Mater. Des. 193 (2020) 108852, https://doi.org/10.1016/j.matdes.2020.108852.

[47] S.-H. Sun, K. Hagihara, T. Nakano, Effect of scanning strategy on texture formation in Ni-25 at%Mo alloys fabricated by selective laser melting, Mater. Des. 140 (2018) 307–316, https://doi.org/10.1016/j.matdes.2017.11.060.

[48] M. Haines, F. List, K. Carver, D. Leonard, A. Plotkowski, C. Fancher, R. Dehoff, S. Babu, Role of scan strategies and heat treatment on grain structure evolution in Fe-Si soft magnetic alloys made by laser-powder bed fusion, Addit. Manuf. 50 (2022) 102578, https://doi.org/10.1016/j.addma.2021.102578.

[49] S. Huang, P. Kumar, W.Y. Yeong, R.L. Narayan, U. Ramamurty, Fracture behavior of laser powder bed fusion fabricated Ti41Nb via in-situ alloying, Acta Mater. 225 (2022) 117593, https://doi.org/10.1016/j.actamat.2021.117593.

[50] S. Huang, R.L. Narayan, J.H.K. Tan, S.L. Sing, W.Y. Yeong, Resolving the porosity-unmelted inclusion dilemma during in-situ alloying of Ti34Nb via laser powder bed fusion, Acta Mater. 204 (2021) 116522, https://doi.org/10.1016/j.actamat.2020.116522.

[51] L. Yao, S. Huang, U. Ramamurty, Z. Xiao, On the formation of “Fish-scale” morphology with curved grain interfacial microstructures during selective laser melting of dissimilar alloys, Acta Mater. 220 (2021) 117331, https://doi.org/10.1016/j.actamat.2021.117331.

[52] S. Gao, Z. Hu, M. Duchamp, P.S.S.R. Krishnan, S. Tekumalla, X. Song, M. Seita, Recrystallization-based grain boundary engineering of 316L stainless steel produced via selective laser melting, Acta Mater. 200 (2020) 366–377, https://doi.org/10.1016/j.actamat.2020.09.015.

[53] T.H. Becker, P. Kumar, U. Ramamurty, Fracture and fatigue in additively manufactured metals, Acta Mater. 219 (2021) 117240, https://doi.org/10.1016/j.actamat.2021.117240.

[54] J. Radhakrishnan, P. Kumar, S. Li, Y. Zhao, U. Ramamurty, Unnotched fatigue of Inconel 718 produced by laser beam-powder bed fusion at 25 and 600°C, Acta Mater. 225 (2022) 117565, https://doi.org/10.1016/j.actamat.2021.117565.

[55] M. Matsumoto, M. Shiomi, K. Osakada, F. Abe, Finite element analysis of single layer forming on metallic powder bed in rapid prototyping by selective laser processing, Int. J. Mach. Tools Manuf. 42 (2002) 61–67, https://doi.org/10.1016/S0890-6955(01)00093-1.

[56] P. Mercelis, J. Kruth, Residual stresses in selective laser sintering and selective laser melting, Rapid Prototyp. J. 12 (2006) 254–265, https://doi.org/10.1108/13552540610707013.

[57] K.A. Liogas, K.B. Lau, Z. Wang, D.N. Brown, E. Polatidis, P. Wang, A.M. Korsunsky, Effect of heat treatment on the microstructure and magnetic properties of laser powder bed fusion processed equiatomic Co-Fe, Addit. Manuf. 67 (2023) 103499, https://doi.org/10.1016/j.addma.2023.103499.

[58] Hiperco_50A_Alloy_(E199).pdf, (n.d.). ⟨https://f.hubspotusercontent20.net/hubfs/7407327/carpenter_electrification/Resources/Datasheets/Hiperco_50A_Alloy_(E199).pdf⟩ (accessed April 24, 2023).

[59] Downloads | VAC, (n.d.). ⟨https://vacuumschmelze.de/shared/quickNav/Downloads⟩ (accessed April 24, 2023).

[60] A. Plotkowski, K. Carver, F. List, J. Pries, Z. Li, A.M. Rossy, D. Leonard, Design and performance of an additively manufactured high-Si transformer core, Mater. Des. 194 (2020) 108894, https://doi.org/10.1016/j.matdes.2020.108894.

[61] A. Plotkowski, J. Pries, F. List, P. Nandwana, B. Stump, K. Carver, R.R. Dehoff, Influence of scan pattern and geometry on the microstructure and soft-magnetic performance of additively manufactured Fe-Si, Addit. Manuf. 29 (2019) 100781, https://doi.org/10.1016/j.addma.2019.100781.

[62] J.M. Adamczyk, S.E. Birchall, E.T. Rothermel, S.R. Whetten, E.J. Barrick, C. J. Pearce, R.E. Delaney, J.W. Pegues, K.L. Johnson, D.F. Susan, T.C. Monson, A. B. Kustas, Characterization of Fe-6Si soft magnetic alloy produced by laser-directed energy deposition additive manufacturing, JOM 76 (2024) 863–874, https://doi.org/10.1007/s11837-023-06293-5.

[63] I. Ohnuma, S. Abe, S. Shimenouchi, T. Omori, R. Kainuma, K. Ishida, Experimental and thermodynamic studies of the Fe–Si binary system, ISIJ Int 52 (2012) 540–548, https://doi.org/10.2355/isijinternational.52.540.

[64] Standard Test Method for Direct Current Magnetic Properties of Low Coercivity Magnetic Materials Using Hysteresigraphs, (n.d.). ⟨https://www.astm.org/a0773_a0773m-21.html⟩ (accessed September 24, 2023).

[65] J.-K. Jung, Y.-J. Park, N.-M. Hwang, Y.-C. Joo, Tertiary grain growth driven by surface energy, Scr. Mater. 45 (2001) 267–272, https://doi.org/10.1016/S1359-6462(01)01017-X.

[66] S. Gao, H. Liao, X. Yan, Y. Yang, J. Wang, C. Chang, Q. Chu, Z. Deng, B. Lu, M. Liu, N. Feneniche, Effects of heat treatment on the microstructures and magnetic properties of selective laser melted Fe-3 wt%Si functional soft magnet, J. Alloy. Compd. 951 (2023) 169840, https://doi.org/10.1016/j.jallcom.2023.169840.

[67] S. Kou. Welding Metallurgy, second ed., Wiley-Interscience, Hoboken, N.J, 2003.

[68] B. Dovgyy, M. Simonelli, M.-S. Pham, Alloy design against the solidification cracking in fusion additive manufacturing: an application to a FeCrAl alloy, Mater. Res. Lett. 9 (2021) 350–357, https://doi.org/10.1080/21663831.2021.1922945.

[69] T. Nozawa, M. Mizogami, H. Mogi, Y. Matsuo, Magnetic properties and dynamic domain behavior in grain-oriented 3% Si-Fe, IEEE Trans. Magn. 32 (1996) 572–589.

[70] R.H. Yu, S. Basu, L. Ren, Y. Zhang, A. Parvizi-Majidi, K.M. Unruh, J.Q. Xiao, High temperature soft magnetic materials: FeCo alloys and composites, IEEE Trans. Magn. 36 (2000) 3388–3393, https://doi.org/10.1109/20.908809.

[71] B. Westerstrand, P. Nordblad, L. Nordborg, The magnetocrystalline anisotropy constants of iron and iron-silicon alloys, Phys. Scr. 11 (2007) 383, https://doi.org/10.1088/0031-8949/11/6/010.

[72] F. Fiorillo, G. Bertotti, C. Appino, M. Pasquale, Soft Magnetic Materials, in: Wiley Encyclopedia of Electrical and Electronics Engineering, John Wiley & Sons, Inc., Hoboken, NJ, USA, 1999: pp. 1–42. https://doi.org/10.1002/047134608X.W4504.pub2.